

## MOX-Report No. 64/2025

# Cardiocirculatory Computational Models for the Study of Hypertension

Celora, S.; Tonini, A.; Regazzoni, F.; Dede', L. Parati, G.; Quarteroni, A.

MOX, Dipartimento di Matematica Politecnico di Milano, Via Bonardi 9 - 20133 Milano (Italy)

mox-dmat@polimi.it

https://mox.polimi.it

# Cardiocirculatory Computational Models for the Study of Hypertension

Simone Celora<sup>1</sup>, Andrea Tonini<sup>2</sup>, Francesco Regazzoni<sup>2</sup>, Luca Dede'<sup>2</sup>, Gianfranco Parati<sup>3,4</sup>, and Alfio Quarteroni<sup>2,5</sup>

<sup>1</sup>Politecnico di Milano, Piazza Leonardo da Vinci 32, 20133 Milano, Italy
 <sup>2</sup>MOX, Department of Mathematics, Politecnico di Milano,, Piazza Leonardo da Vinci 32, 20133 Milano, Italy

<sup>3</sup>Department of Cardiology, S.Luca Hospital, IRCCS, Istituto Auxologico Italiano,, Piazzale Brescia 20, 20149 Milano, Italy

<sup>4</sup>Department of Medicine and Surgery, University of Milano-Bicocca,, via Vizzola 5, 20126 Milano, Italy

<sup>5</sup>Institute of Mathematics, École Polytechnique Fédérale de Lausanne,, Station 8, Av. Piccard, CH-1015 Lausanne, Switzerland

October 16, 2025

#### Abstract

In this work, we develop patient-specific cardiocirculatory models with the aim of building Digital Twins for hypertension. In particular, in our pathophysiology-based framework, we consider both 0D cardiocirculatory models and a 3D-0D electromechanical model. The 0D model, which consists of an RLC circuit, is studied in two variants, with and without capillaries. The 3D-0D model consists of a three-dimensional electromechanical model of the left ventricle, coupled with a 0D model for the external blood circulation: this representation enables the assessment of additional quantities related to ventricular deformation and stress, and offers a more detailed representation compared to a fully 0D model. Sensitivity analysis is performed on the 0D model, with both a mono- and a multi-parametric approach, in order to identify the parameters that most influence the model outputs and guide the calibration process. We studied three different scenarios, corresponding to systemic, pulmonary and renovascular hypertension, each in three nuances of severity. To maintain a fair comparison among the models, a parameter calibration strategy is developed; the outputs of the 0D model with capillaries are utilized to enhance the 3D-0D model. The results demonstrate that the 3D-0D model yields an accurate representation of cardiocirculatory dynamics in the presence of hypertension; this model represents a powerful step toward digital twins for real-time hypertension control, providing refined and clinically meaningful insights beyond those achievable with 0D models alone.

**Keywords:** Cardiovascular Modeling; Hypertension; Digital Twins; Hypertension Simulation; Ventricular Electromechanics; Sensitivity Analysis; Parameter Calibration

#### 1 Introduction

Hypertension, along with higher than normal or elevated blood pressure levels, is one of the world's leading risk factors for death and disability [1, 2], since it may cause stroke, ischaemic heart disease, altered vascular conditions and kidney disorders [3, 4]. High systolic blood pressure is responsible for more deaths than any other health risk. According to [1], it accounted for over 10 million deaths annually and contributed to over half of all cardiocirculatory-related deaths worldwide in 2019 [5]; furthermore, in less than 30 years, the number of hypertensive individuals doubled: from 650 million in 1990 to 1.3 billion in 2019 [6]. According to the most recent World Health Organization report [2]

"in 2024, an estimated 1.4 billion people aged 30–79 years were affected worldwide, yet fewer than 1 in 5 (320 million) had the condition adequately controlled".

Hypertension is often referred to as the "silent killer" because it is typically asymptomatic: unless blood pressure is measured, most individuals remain unaware of their condition until they experience a clinical complication, i.e. heart attack, stroke or kidney failure. Proper management of hypertension requires accurate diagnosis, prompt initiation of treatment in severe cases and continuous monitoring of progress. Timelines are crucial: the longer a person suffers from undiagnosed or poorly managed hypertension, the worse the health consequences are likely to be [1, 2].

Due to hypertension profound impact on global health, a comprehensive understanding of this condition is crucial. Mathematical models are increasingly recognized as indispensable tools for studying complex physiological phenomena, offering insights that traditional approaches alone may not provide. Within this context, the concept of Digital Twins (DTs) is gaining ground in cardiovascular research [7, 8]. Unlike a simple patient-specific model, a digital twin establishes a continuous interaction between the physical and digital entities: patient data drive the calibration of the computational model, while the predictions obtained from the model can guide clinical choices, such as the selection of therapeutic strategies [9]. By integrating clinical and sensor data into mathematical models, DTs allow simulations tailored to the individual patient, enabling accurate reproduction of haemodynamics and prediction of disease progression. Hypertension has already been investigated using machine learning models, as evidenced by works such as [10, 11]; nonetheless, there has also been an increasing use of differential equation (DE)-based models to simulate the cardiocirculatory system and study hypertension (e.g. [12, 13]). The use of DE-based models, combined with real patient data, enables the creation of personalized models tailored to individual patients: by incorporating patient-specific physiological information, these models are able to simulate cardiocirculatory haemodynamics with greater accuracy and reflect the unique characteristics of each patient's condition. When combined with real patient data, such DE-based models naturally lend themselves to the construction of DTs, as they can reproduce patient-specific cardiocirculatory dynamics and reflect the unique characteristics of individual conditions.

Albeit advanced and complex models are increasingly being used as complementary tools to the study of pathological conditions, hypertension modeling has been little explored in literature. This paper is proposed as an innovative contribution in this direction, providing a framework that not only simulates different forms of hypertension but also provides a foundation for future developments toward cardiovascular DTs. The adopted approach, which combines lumped-parameter models and detailed electromechanical representations, makes it possible to explore the dynamics of the cardiocirculatory system with a hitherto little studied level of detail: the current work stands as a forerunner in the modeling of hypertension, helps to fill a gap in the existing literature and supports the advancement of patient-specific DTs for predictive and personalized analysis.

Several differential mathematical and numerical models are employed to analyze the dynamics of hypertension, simulate its effects under various conditions and compare the simulated outputs with clinically observed trends and reference values from the literature: in particular, a lumped-parameter cardiocirculatory model (from now on referred to as (%) or 0D model), based on a 0D representation by an RLC circuit, and an electromechanical model ([14]) coupled with a lumped-parameter model (from now on referred to as 3D-0D model), where the left ventricle is represented in 3D through sophisticated electromechanical modeling, coupled with a 0D model of the blood circulation. The integrated approach not only enhances the understanding of hypertension, but also contributes to the development of improved diagnostic, therapeutic and preventive strategies, within a DT framework. Through the proposed modeling framework, the simulations reproduce the haemodynamic alterations associated with various forms and grades of hypertension; the results show the effect of increased vascular resistance and reduced compliance on both systemic and pulmonary circulation, demonstrating how these changes deeply affect pressure dynamics and cardiac workload. Furthermore, the comparison between 0D and 3D-0D models yields valuable insights into advantages and limitations of each approach, emphasizing the importance of patient-specific modeling for an accurate representation of hypertensive conditions.

The current paper is organized as follows: Section 2 provides a clinical overview of hypertension,

with a brief description of its causes and effects; in Section 3, the employed mathematical models are presented, along with an analysis of the relevant parameters involved; Section 4 illustrates the implementation of different kinds of hypertension within the mathematical framework, with a description of the necessary modifications and assumptions for correct modeling; Section 5 is devoted to numerical results obtained from the simulations, comparison of the model outputs with real-world clinical data and evaluation of their consistency; finally, conclusions follow in Section 6.

## 2 Pathophysiology of Hypertension

In accordance with the 2023 European and current international guidelines [15], hypertension is diagnosed when office blood pressure measurements (i.e. taken in a clinical or healthcare setting) is equal or higher than 140 mmHg for systolic blood pressure or 90 mmHg for diastolic blood pressure, although recent USA guidelines have adopted a lower threshold, i.e. equal or higher than 130/80 mmHg. Alternative definitions are considered to identify related conditions such as pulmonary hypertension, as described below. Hypertension can be classified in several ways considering aspects such as the underlying causes, the severity of blood pressure elevation, the timing and consistency of measurements, the presence of associated complications, or other risk factors. An important distinction is made between primary and secondary hypertension: while primary hypertension has no clearly identifiable cause and accounts for the vast majority of cases, secondary hypertension arises from specific, diagnosable medical conditions (e.g. renal, endocrine or vascular disorders) [16]. Hypertension can be further classified based on its origin and the vascular district involved. Here, the forms that are more related to this work are briefly described:

- 1. systemic hypertension refers to elevated pressure in the systemic circulation and is the most common form [16]. It is typically associated with increased peripheral resistance and large artery stiffening, affecting left ventricular function and contributing to long-term cardiovascular damage;
- 2. pulmonary hypertension by contrast, is defined as a mean pulmonary artery pressure above 20 mmHg at rest [17]. It affects the pulmonary circulation and can be caused by a variety of mechanisms, including left heart dysfunction, lung diseases, hypoxia exposure, or vascular abnormalities. It leads to increased right ventricular workload and is associated with a high morbidity and mortality risk;
- 3. renovascular hypertension is a form of secondary hypertension caused by reduced renal perfusion, most commonly due to atherosclerotic renal artery stenosis or fibromuscular dysplasia [18]. The decrease in renal blood flow promotes renin secretion, vasoconstriction, sympathetic stimulation and fluid retention, all of which contribute to a sustained elevation in systemic blood pressure.

#### 2.1 Etiology and Clinical Manifestations

Hypertension is a multifactorial condition with both genetic and environmental influences. It may be asymptomatic in its early stages but can lead to progressive damage to key organs such as the heart, brain, vasculature and kidneys as blood pressure rises [19]. Hypertensive individuals often exhibit enhanced vasoconstriction in both large and small arteries. This phenomenon, alongside the increase in blood pressure, appears to be favored by systemic autoregulation, triggered by the preliminary increase of blood volume and cardiac output; this mechanism refers to the ability of blood vessels to maintain a constant blood flow, despite changes in blood pressure [20]. Hypertension is very commonly associated with impaired vasodilation, due mostly to endothelial dysfunction and structural changes in blood vessels [21]. In small vessels, remodeling of arterioles results in smooth muscle layer thickening and lumen narrowing, increasing overall vascular resistance [22]. Other studies documented a two-way relation between aortic stiffness and hypertension, as one condition increases due to the other one in a self-promoting circle. A known impact of stiffness is the transmission of pressure into the smaller vessels, which may cause harm to the organs [23].

Chronic high blood pressure puts stress on the left ventricular wall by increasing the afterload, promoting left ventricular remodeling and hypertrophy; the latter is a well-established risk factor for adverse cardiocirculatory outcomes, such as myocardial infarction, heart failure, atrial fibrillation, stroke and cardiocirculatory mortality [19]. Long-term elevated pressure in the left ventricle may lead to the dysfunction of the left atrium through dilation. There is ample evidence linking hypertension with the etiology of valvular heart disease [24]: an increased systolic blood pressure has been associated with an elevated risk of conditions such as aortic stenosis and aortic regurgitation. The effects of hypertension involve endothelial dysfunction, vascular remodeling and enhanced vascular stiffness, which not only contribute to the development of the disease, but are also results of it in turn [25]. The kidney is also a key actor in the development and sustainment of hypertension: regulating systemic vasoconstriction and blood pressure through both direct hormonal actions and feedback mechanisms, including fluid balance, sodium handling and sympathetic activity [26, 27]. Hypertension and chronic kidney disease are closely linked in a complex relationship: the former can be considered both a cause and a consequence of the latter, promoting its progression [28].

# 3 Differential Mathematical Models for the Cardiocirculatory System

This section provides an overview of the models adopted for this paper, describing their mathematical formulation, the key assumptions, the functionality and the involved parameters [29, 30, 31]. In Section 3.1, the 0D models are illustrated, while the 3D–0D coupled model is described and briefly analyzed in Section 3.2.

#### 3.1 A 0D Model for Closed-Loop Blood Circulation

The 0D model ( $\mathscr{C}$ ) [29, 31] describes the haemodynamics of the cardiocirculatory system by means of a lumped-parameter approach: it represents the entire circulatory network as a set of 0D interconnected components, and allows the system to be modeled using ordinary differential equations (ODEs). ( $\mathscr{C}$ ) is based on the assumption that the cardiocirculatory system can be simplified into discrete elements that capture the mean features of blood flow and pressure dynamics. This type of models have been implemented in two variants (Figure 1a): ( $\mathscr{C}_{\rm C}$ ) which includes capillaries and ( $\mathscr{C}_{\rm NC}$ ) which does not. The circulation is simulated over a time period T, long enough to reach a periodic limit cycle in the output variables, with period that of the cardiac cycle; this periodicity is a property of the simulation rather than the model itself. Only results belonging to the last heartbeat, lasting  $T_{\rm HB}$ , are then considered.

In (%), both the systemic and pulmonary circulations are represented by a resistance-inductance capacitance (RLC) circuit: the resistance corresponds to the opposition to blood flow, the inductance accounts for the inertial effects of the blood, and the capacitance represents the elasticity of the vessel walls. The heart is modeled as a series of time-varying elastance elements, describing dynamic variations of the force developed by the cardiac muscle during the cardiac cycle. Such elements characterize each of the four cardiac chambers, allowing for the simulation of contraction and relaxation phases of the heart. The four heart valves are represented as non-ideal diodes: they capture the unidirectional blood flow and the resistance to backflow when the valves are closed. The heart elements are integrated into a closed-loop system, where the interactions between the heart and the blood vessels are modeled to replicate the complete haemodynamic behaviour of the cardiocirculatory system.

The two variations of the model are based on distinct systems of ODEs, reflecting the inclusion or exclusion of capillaries; below, the system of ODEs for  $(\mathcal{C}_{NC})$  is presented:

$$\frac{dV_{\rm RA}(t)}{dt} = Q_{\rm VEN}^{\rm SXS}(t) - Q_{\rm TV}(t),$$

$$\frac{dV_{\rm LA}(t)}{dt} = Q_{\rm VEN}^{\rm VEN}(t) - Q_{\rm PV}(t),$$

$$\frac{dV_{\rm LA}(t)}{dt} = Q_{\rm TV}(t) - Q_{\rm PV}(t),$$

$$\frac{dV_{\rm LN}(t)}{dt} = Q_{\rm TV}(t) - Q_{\rm PV}(t),$$

$$\frac{dV_{\rm LN}(t)}{dt} = Q_{\rm LN}(t) - Q_{\rm AN}(t),$$

$$\frac{dV_{\rm LN}(t)}{dt} = Q_{\rm LN}(t) - Q_{\rm VEN}^{\rm DIL}(t),$$

$$\frac{dV_{\rm LN}(t)}{dt} = Q_{\rm LN}(t) - Q_{\rm VEN}^{\rm DIL}(t),$$

$$\frac{dV_{\rm LN}(t)}{dt} = Q_{\rm LN}(t) - Q_{\rm VEN}^{\rm DIL}(t),$$

$$\frac{dV_{\rm LN}(t)}{dt} = Q_{\rm LN}(t) - Q_{\rm VEN}^{\rm DIL}(t),$$

$$\frac{dV_{\rm LN}(t)}{dt} = Q_{\rm LN}(t) - Q_{\rm VEN}^{\rm DIL}(t),$$

$$\frac{dV_{\rm LN}(t)}{dt} = Q_{\rm LN}(t) - Q_{\rm LN}^{\rm PUL}(t),$$

$$\frac{dV_{\rm LN}(t)}{dt} = Q_{\rm LN}(t) - Q_{\rm LN}^{\rm PUL}(t),$$

$$\frac{dV_{\rm LN}(t)}{dt} = Q_{\rm LN}(t) - Q_{\rm LN}^{\rm PUL}(t),$$

$$\frac{dV_{\rm LN}(t)}{dt} = Q_{\rm LN}(t) - Q_{\rm LN}^{\rm PUL}(t),$$

$$\frac{dV_{\rm LN}(t)}{dt} = Q_{\rm LN}(t) - Q_{\rm LN}^{\rm PUL}(t),$$

$$\frac{dV_{\rm LN}(t)}{dt} = Q_{\rm LN}(t) - Q_{\rm LN}^{\rm PUL}(t),$$

$$\frac{dV_{\rm LN}(t)}{dt} = Q_{\rm LN}(t) - Q_{\rm LN}^{\rm PUL}(t),$$

$$\frac{dV_{\rm LN}(t)}{dt} = Q_{\rm LN}(t) - Q_{\rm LN}^{\rm PUL}(t),$$

$$\frac{dV_{\rm LN}(t)}{dt} = Q_{\rm LN}(t) - Q_{\rm LN}^{\rm PUL}(t),$$

$$\frac{dV_{\rm LN}(t)}{dt} = Q_{\rm LN}(t) - Q_{\rm LN}^{\rm PUL}(t),$$

$$\frac{dV_{\rm LN}(t)}{dt} = Q_{\rm LN}(t) - Q_{\rm LN}^{\rm PUL}(t),$$

$$\frac{dV_{\rm LN}(t)}{dt} = Q_{\rm LN}(t) - Q_{\rm LN}^{\rm PUL}(t),$$

$$\frac{dV_{\rm LN}(t)}{dt} = Q_{\rm LN}(t) - Q_{\rm LN}^{\rm PUL}(t),$$

$$\frac{dV_{\rm LN}(t)}{dt} = Q_{\rm LN}(t) - Q_{\rm LN}^{\rm PUL}(t),$$

$$\frac{dV_{\rm LN}(t)}{dt} = Q_{\rm LN}(t) - Q_{\rm LN}^{\rm PUL}(t),$$

$$\frac{dV_{\rm LN}(t)}{dt} = Q_{\rm LN}(t) - Q_{\rm LN}^{\rm PUL}(t),$$

$$\frac{dV_{\rm LN}(t)}{dt} = Q_{\rm LN}(t) - Q_{\rm LN}(t),$$

for  $t \in (0,T]$ , and coupled with suitable initial conditions.

 $(\mathscr{C}_{\mathcal{C}})$  introduces modifications to Equations (1c) and (1f), respectively:

$$\frac{dp_{\mathrm{VEN}}^{\mathrm{SYS}}(t)}{dt} = \frac{Q_{\mathrm{C}}^{\mathrm{SYS}}(t) - Q_{\mathrm{VEN}}^{\mathrm{SYS}}(t)}{C_{\mathrm{VEN}}^{\mathrm{SYS}}}, \qquad \frac{dp_{\mathrm{VEN}}^{\mathrm{PUL}}(t)}{dt} = \frac{Q_{\mathrm{SH}}(t) + Q_{\mathrm{C}}^{\mathrm{PUL}}(t) - Q_{\mathrm{VEN}}^{\mathrm{PUL}}(t)}{C_{\mathrm{VEN}}^{\mathrm{PUL}}}, \qquad (2c)$$

$$\frac{dQ_{\mathrm{AR}}^{\mathrm{PUL}}(t)}{dt} = -\left(Q_{\mathrm{AR}}^{\mathrm{PUL}}(t) + \frac{p_{\mathrm{C}}^{\mathrm{PUL}}(t) - p_{\mathrm{AR}}^{\mathrm{PUL}}(t)}{R_{\mathrm{AR}}^{\mathrm{PUL}}}\right) \frac{R_{\mathrm{AR}}^{\mathrm{PUL}}}{L_{\mathrm{AR}}^{\mathrm{PUL}}}, \qquad \frac{dQ_{\mathrm{AR}}^{\mathrm{SYS}}(t)}{dt} = -\left(Q_{\mathrm{AR}}^{\mathrm{SYS}}(t) + \frac{p_{\mathrm{C}}^{\mathrm{SYS}}(t) - p_{\mathrm{AR}}^{\mathrm{SYS}}(t)}{R_{\mathrm{AR}}^{\mathrm{SYS}}}\right) \frac{R_{\mathrm{AR}}^{\mathrm{SYS}}}{L_{\mathrm{AR}}^{\mathrm{SYS}}}, \qquad (2f)$$

for  $t \in (0,T]$ , and adds the additional ones, here presented:

$$\frac{dp_{\mathrm{C}}^{\mathrm{SYS}}(t)}{dt} = \frac{Q_{\mathrm{AR}}^{\mathrm{SYS}}(t) - Q_{\mathrm{C}}^{\mathrm{SYS}}(t)}{C_{\mathrm{C}}^{\mathrm{SYS}}}, \qquad \frac{dp_{\mathrm{C}}^{\mathrm{PUL}}(t)}{dt} = \frac{Q_{\mathrm{AR}}^{\mathrm{PUL}}(t) - Q_{\mathrm{SH}}(t) - Q_{\mathrm{C}}^{\mathrm{PUL}}(t)}{C_{\mathrm{C}}^{\mathrm{PUL}} + C_{\mathrm{SH}}}, \qquad (2g)$$

for  $t \in (0,T]$ , to account for the haemodynamics of the capillary network, while the others remain unchanged between the two models.

In both the models, the pressures in the four heart chambers are computed as:

$$p_i(t) = p_{\text{EX}}(t) + E_i(t) (V_i(t) - V_{0,i}), \quad i \in \{\text{LA, LV, RA, RV}\},$$
 (3)

while the fluxes through the four heart valves are defined as:

$$Q_{\text{TV}}(t) = \frac{p_{\text{RA}}(t) - p_{\text{RV}}(t)}{R_{\text{TV}}(p_{\text{RA}}(t), p_{\text{RV}}(t))}, \qquad Q_{\text{PV}}(t) = \frac{p_{\text{RV}}(t) - p_{\text{AR}}^{\text{PUL}}(t)}{R_{\text{MV}}(p_{\text{RV}}(t), p_{\text{PUL}}^{\text{PUL}}(t))}, \qquad (4a)$$

$$Q_{\rm MV}(t) = \frac{p_{\rm LA}(t) - p_{\rm LV}(t)}{R_{\rm MV}(p_{\rm LA}(t), p_{\rm LV}(t))}, \qquad Q_{\rm AV}(t) = \frac{p_{\rm LV}(t) - p_{\rm AR}^{\rm SYS}(t)}{R_{\rm AV}(p_{\rm LV}(t), p_{\rm AR}^{\rm SYS}(t))}, \tag{4b}$$

where  $V_{0,i}$  is the resting volume of heart chamber i;  $p_{EX}(t)$  is the pressure exerted outside the heart by the surrounding organs and respiration, and in this work will always be set to 0.

Equations (2c), (2f) and (2g) introduce the following new flux variables:

$$Q_{\rm C}^{\rm SYS} = \frac{p_{\rm C}^{\rm SYS}(t) - p_{\rm VEN}^{\rm SYS}(t)}{{\rm R}_{\rm C}^{\rm SYS}}, \qquad Q_{\rm C}^{\rm PUL} = \frac{p_{\rm C}^{\rm PUL}(t) - p_{\rm VEN}^{\rm PUL}(t)}{{\rm R}_{\rm C}^{\rm PUL}}, \qquad Q_{\rm SH} = \frac{p_{\rm C}^{\rm PUL}(t) - p_{\rm VEN}^{\rm PUL}(t)}{{\rm R}_{\rm SH}}. \tag{5}$$

A compact representation suitable for both the 0D models is provided here:

$$\begin{pmatrix}
\frac{d\mathbf{c}_{1}(t)}{dt} = \mathbf{D}(t, \mathbf{c}_{1}(t), \mathbf{c}_{2}(t)) & \text{for } t \in (0, T], \\
\mathbf{c}_{2}(t) = \mathbf{W}(t, \mathbf{c}_{1}(t)) & \text{for } t \in [0, T], \\
\mathbf{c}_{1}(0) = \mathbf{c}_{1,0}.
\end{pmatrix} \tag{6}$$

The same notation of Equation (6) can be used to represent both ( $\mathscr{C}_{\mathbb{C}}$ ) and ( $\mathscr{C}_{\mathbb{NC}}$ ).

#### 3.2 The 3D Electromechanical Model coupled with the Lumped-Parameter Model

The 3D–0D model employed in this paper is the one presented in [29], which couples a detailed 3D electromechanical model of the left ventricle with a 0D model of the systemic and pulmonary circulations. The 3D left ventricle is represented by the computational domain  $\Omega_0 \subset \mathbb{R}^3$ , with its boundary  $\partial\Omega_0$  being split into three distinct sections: the endocardium ( $\Gamma_0^{\text{endo}}$ ), the epicardium ( $\Gamma_0^{\text{epi}}$ ) and the ventricular base ( $\Gamma_0^{\text{base}}$ ); the latter represents the artificial boundary where the left ventricle geometry is cut.

The multiphysics and multiscale model of cardiac electromechanics comprises five separate core models:

- 1. transmission of cardiac electrical potential  $(\mathcal{E})$ ;
- 2. ion dynamics  $(\mathcal{I})$ ;
- 3. contraction of cardiac muscle cells  $(\mathscr{A})$ ;
- 4. mechanical behaviour of tissue  $(\mathcal{M})$ ;
- 5. blood circulation ( $\mathscr{C}$ ).

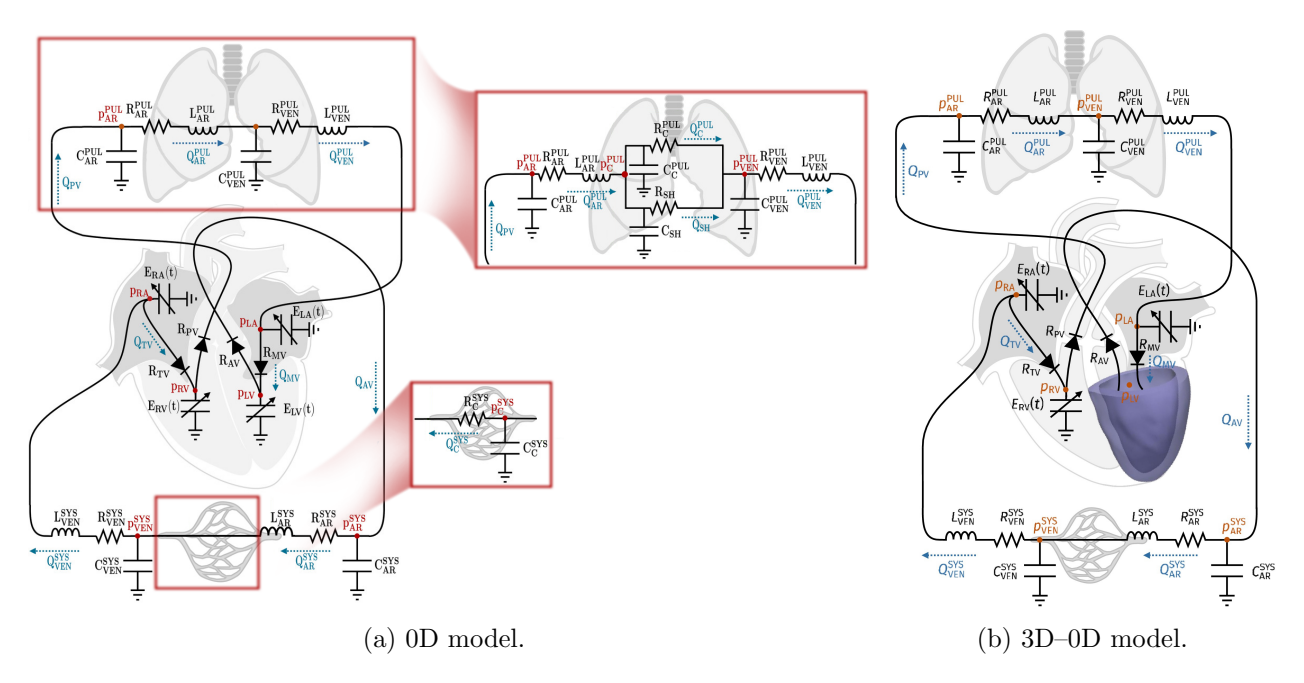


Figure 1: 0D cardiocirculatory models with (center) and without (left) capillaries. The 3D–0D coupling between the left ventricle 3D electromechanical model and the 0D circulation model without capillaries is shown on the right. Source: [29, 31] and graphical modifications.

These core models capture the various physical processes involved in cardiac function, at different spatial and temporal dimensions. Furthermore, a volume conservation constraint ( $\mathcal{V}$ ) ensures the proper interaction between ( $\mathcal{M}$ ) and ( $\mathcal{C}$ ). In Figure 1b, the complete 3D–0D model is presented. Such a model includes multiple unknowns, depending on both time and space, that represent the variables related to each core model and describe the interactions between them; u denotes the transmembrane potential, w and z represent the ionic variables, s indicates the state variables of the force generation model, d refers to the mechanical displacement of the tissue,  $c_1$  is the state vector of the circulation model, and  $p_{IN}$  represents the pressure of left ventricle.

The 3D–0D complete model is defined by sets of partial differential equations (PDEs); the detailed formulation is reported in A. In ( $\mathcal{E}$ ), the dynamics of the transmembrane potential u are captured by a diffusion-reaction PDE, which governs the electrical behaviour of cardiac muscle cells [32, 33, 34]. For the purpose of electromechanic coupling, a proper modeling of the ionic fluxes across the cell membrane is mandatory [35]; the latter involves the inclusion of two variables: the recovery variables  $\boldsymbol{w}$ , which characterize the proportion of open ionic channels, and the concentration variables  $\boldsymbol{z}$ , describing the concentrations of critical ionic species, such as intracellular calcium ions  $\left[\operatorname{Ca}^{2+}\right]_i$ , which play a pivotal role in triggering mechanical contraction.

In the electrophysiological framework defined by  $(\mathscr{E}) - (\mathscr{I})$ , the transmembrane potential u propagates through gap junctions; this phenomenon is governed by the diffusion term  $\nabla \cdot (J\mathbf{F}^{-1}\mathbf{D}_{\mathbf{M}}\mathbf{F}^{-T}\nabla u)$ , which incorporates the influence of tissue deformation and introduces a feedback mechanism, linking electrical behaviour to mechanical stretch. Here,  $\mathbf{F} = \mathbf{I} + \nabla d$  is the deformation gradient tensor, while  $\mathbf{D}_{\mathbf{M}}$  represents the diffusion tensor, which captures the anisotropic characteristics of cardiac tissue. The applied current,  $\mathcal{I}_{\mathrm{app}}(t)$ , simulates the role of the Purkinje network: these fibers form the outermost component of the cardiac conduction system and their primary function is to ensure the swift and synchronized activation of the ventricular myocardium [36]. Additionally, the ionic current  $\mathcal{I}_{\mathrm{ion}}(u, \boldsymbol{w}, \boldsymbol{z})$  encapsulates multiscale interactions at both cellular and tissue levels. Electrically isolated interfaces are modeled using homogeneous Neumann boundary conditions.

Cardiac contraction arises from interactions between actin and myosin proteins within sarcomeres, the fundamental contractile units of heart muscle [37]. To simulate the mechanism in ( $\mathscr{A}$ ), the RDQ20-MF model has been employed [38] instead of RDQ18 in [29]: it provides a complete biophysical model that characterizes the behaviour of sarcomeric proteins, along with the causes that support the responsiveness of the heart towards variations in calcium levels. RDQ20-MF is a system of differential

equations, where the state variables are represented by the vector s; it outputs the permissivity P, representing the fraction of contractile units in the force-generating state, from which the effective active tension  $T_a$  is derived. Inputs to the model include calcium concentration  $[Ca^{2+}]_i$  (properly described using a ionic model), sarcomere length (SL) and its time derivative from the mechanical model.

Tissue displacement d is described by the momentum conservation equation ( $\mathcal{M}$ ). The Piola-Kirchhoff stress tensor  $\mathbf{P}$  represents both the passive and active mechanical properties of the tissue. Under the assumption of hyperelasticity, the passive component of the stress tensor is derived from the strain energy density function  $\mathcal{W}$ , while the active component depends on tissue stretch along the fiber direction and on the active tension  $T_a$ . To capture the anisotropic properties of cardiac muscle, the Guccione strain energy density function as  $\mathcal{W}(\mathbf{F})$  [39, 40] is used, which depends on the Green-Lagrange strain energy tensor. Additionally, to penalize large volume variations and enforce weak incompressibility, a term involving  $J = \det \mathbf{F}$  is added to  $\mathcal{W}(\mathbf{F})$  [41].

To model the interaction between the left ventricle and the pericardium [42], a generalized Robin boundary condition is applied on the epicardium  $\Gamma_0^{\rm epi}$ : this condition is designed to simulate the effect of the right ventricle, major veins and arteries, i.e. to restrict rigid rotations of the ventricle around the apico-basal axis (the direction from the base of the heart to its apex), while permitting torsion. At the base  $\Gamma_0^{\rm base}$ , an energy-consistent boundary condition is enforced: this ensures the correct stress distribution at the base boundary. For the endocardium  $\Gamma_0^{\rm endo}$ , the applied boundary condition accounts for the pressure  $p_{\rm LV}(t)$ , which reflects the pressure exerted by the blood within the ventricle. Lastly, the mechanical model ( $\mathcal{M}$ ) influences ( $\mathcal{A}$ ) by determining the local sarcomere length (SL); the sarcomeres are aligned with the muscle fibers, so the local sarcomere length directly correlates with the tissue stretch along the fiber direction.

In the 3D–0D coupled framework, the 0D cardiocirculatory model used does not include the capillary network. The 0D model, as introduced in Section 3.1, represents each cardiac chamber as a time-varying elastance element and yields a simplified 0D representation of the circulatory system. However, the coupled model integrates this 0D circulatory model with the 3D left ventricular model, which is governed by equations  $(\mathcal{E})$ ,  $(\mathcal{I})$ ,  $(\mathcal{A})$  and  $(\mathcal{M})$ . To achieve this integration, the elastance element of the left ventricle is removed from the 0D model and replaced by the 3D electromechanical model. Additionally, the 3D–0D coupled model must satisfy a volume consistency condition  $\forall t \in (0,T]$ , as described by Equation (14f);  $V_{\rm LV}^{\rm 0D}(\boldsymbol{c}(t))$  and  $V_{\rm LV}^{\rm 3D}(\boldsymbol{d}(t))$  stand for the left ventricular volumes in the 0D and 3D models, respectively. The introduction of this volume-consistency condition leads to an additional unknown variable,  $p_{\rm LV}$ , which is no longer determined by Equation (3), but serves as a Lagrange multiplier enforcing the constraint  $(\mathcal{V})$ . Consequently, a "reduced" vector  $\tilde{\boldsymbol{c}}_2$  is defined, where  $\boldsymbol{c}_2^T = (p_{\rm LV}, \tilde{\boldsymbol{c}}_2^T)$ : this allows for the reformulation of Equations (3) and (4) as:

$$\tilde{\boldsymbol{c}}_2(t) = \overset{\sim}{\mathbf{W}} (t, \boldsymbol{c}_1(t), p_{\mathrm{LV}}(t)).$$

As a result, the reduced version of Equation (6) can be expressed as Equation (14e), where the following expression for  $\overset{\sim}{\mathbf{D}}$  is employed:

$$\stackrel{\sim}{\mathbf{D}}\left(t, \boldsymbol{c}_{1}, p_{\mathrm{LV}}
ight) = \mathbf{D}\left(t, \boldsymbol{c}_{1}, \left( egin{matrix} p_{\mathrm{LV}} \ \overset{\sim}{\mathbf{W}}\left(t, \boldsymbol{c}_{1}, p_{\mathrm{LV}}
ight) \end{matrix}
ight).$$

Finally, the coupled 3D–0D model is obtained, as reported in Equation (14), with the number of equations in the model matching the number of unknowns.

In this paper, a left ventricle geometry is utilized, derived from the Zygote Solid 3D heart model [43]; this model represents the  $50^{\text{th}}$  percentile of a healthy Caucasian male in the U.S., reconstructed from a high-resolution computed tomography scan. The model is acquired at 70% of diastole and captures the late phase of diastasis when passive filling of the ventricles has slowed, but before atrial contraction completes active filling. The mesh used, denoted as  $\mathcal{T}_h$ , consists of 6079 vertices, 6682 triangles and 27492 tetrahedra, with an average element size  $h_{\text{mean}} = 3.7 \text{ mm}$ . The numerical methods, as briefly introduced above, are implemented within the life\* [44, 45] framework in a parallel environment, that utilizes high-performance computing (HPC) resources (total available: 48 Intel Xeon

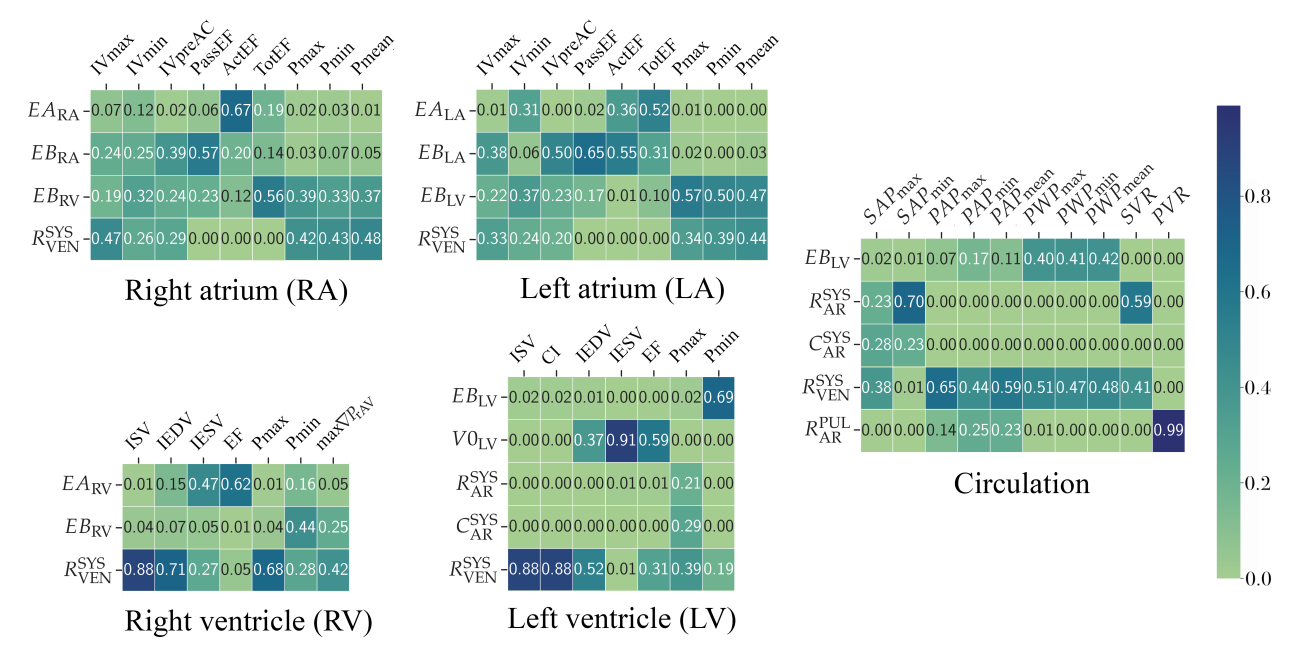


Figure 2: Most relevant total Sobol indices, computed for  $(\mathscr{C}_{NC})$ . The index  $\mathcal{S}_k^{j,\mathcal{T}}$  in position (k,j) quantify the contribution of parameter  $p_k$  to the output  $y_j$ . Only  $\mathcal{S}_k^{j,\mathcal{T}} \geq 0.2$  are shown.

ES-2640 CPUs) at MOX, Politecnico di Milano. For more details about life<sup>x</sup>, its documentation can be retrieved here, while refer to [46] for the last updates.

## 4 Computational Models in Hypertension

In this section, the computational models used to investigate hypertensive conditions are analyzed, focusing on their applicability in reproducing clinically relevant haemodynamic behaviours.

#### 4.1 Sensitivity Analysis in 0D Models

The sensitivity analysis of the 0D models is performed to identify the most influential parameters on the outputs of interest. This analysis is conducted using single- and multi-parameter approaches, respectively in Sections 4.1.1 and 4.1.2.

#### 4.1.1 Single-Parameter Sensitivity Analysis by means of Sobol Indices

Sobol indices [47] are a form of global sensitivity analysis: they rely on the decomposition of the variance of the model's output into components, which correspond to different input variables and their interactions. In this paper, total Sobol indices  $\mathcal{S}_k^{j,\mathcal{T}}$  have been employed: they take into consideration both the direct effect of a parameter  $p_k$  and its interactions with the others. The methodology and analysis of this section are directly derived from [48].

The 0D cardiocirculatory model includes a large number of parameters, however, for practical and methodological reasons, some parameters are not included in the sensitivity analysis: HR is excluded, as can be directly and clinically measured; parameters related to the timings of the cardiac cycle are excluded due to their significant influence on the shape of pressure-volume (PV) loops, as they can lead to non-physical results, and complicate the analysis without providing further insights. Moreover, the total blood volume was not included among the parameters, since in this framework it is implicitly determined by the choice of initial conditions rather than treated as an independent variable. For both  $(\mathcal{C}_{NC})$  and  $(\mathcal{C}_{C})$ , quantification of the influence of parameters and interpretation of their impact on model outputs follow the same principles and hence makes both configurations compatible and comparable.

The  $N_p$  starting parameters, denoted as  $\mathbf{p}^R \in \mathbb{R}^{N_p}$  (B), are selected to be those which generate a simulation for a healthy individual. To simplify the analysis, the parameters are assumed to be independent; furthermore, to reflect the diversity across different healthy and hypertensive individuals, the parameters are allowed to vary in a multidimensional space, a hypercube with its center in  $\mathbf{p}^R$ . The amount of variation along each axis is  $\frac{2}{3}$  of the reference parameter value, therefore each parameter  $p_k$  is sampled within the interval:

$$\mathbf{I}_k = \left[ \left( 1 - \frac{2}{3} \right) p_k^{\mathrm{R}}, \left( 1 + \frac{2}{3} \right) p_k^{\mathrm{R}} \right], \quad k \in \mathbb{N} \text{ and } 1 \leq k \leq \mathbf{N}_p,$$

ensuring the representation of various physiological conditions.

In the parameter sampling process, Sobol sequences are used to ensure a more uniform and spacefilling coverage of the hypercube, by minimizing clustering and gaps. This quasi-random structure allows for faster convergence of the sample mean to the expected value compared to standard Monte Carlo sampling, thereby reducing the number of simulations needed to explore the parameter space effectively [49]. Sobol indices are computed using Saltelli's method [50]: this technique guarantees a high-resolution variance decomposition, providing an accurate information on the contribution of each parameter and its interactions. Though computational effort of Saltelli's method scales linearly with the number of parameters, it is still feasible, since ( $\mathcal{C}_{NC}$ ) and ( $\mathcal{C}_{C}$ ) are computationally cheap, and parallelization limits the time taken for processing. In this paper,  $N_p = 26$  parameters are analyzed for ( $\mathcal{C}_{NC}$ ), while, in the case of ( $\mathcal{C}_{C}$ ), the number of parameters taken in account rises up to 32; the method generates  $2N (N_p + 1)$  samples ( $N = 2^{12}$  is a user-defined value), resulting in 221,184 samples for ( $\mathcal{C}_{NC}$ ) and 270,336 samples for ( $\mathcal{C}_{C}$ ). The most relevant total Sobol indices ( $\geq 0.2$ ) for ( $\mathcal{C}_{NC}$ ), obtained through this procedure and subsequently utilized, are shown in Figure 2.

#### 4.1.2 Multi-Parameter Sensitivity Analysis

Multi-parameter sensitivity analysis extends the traditional sensitivity analysis in order to understand the combined effects that related parameters have on model outputs: this approach aggregates them into meaningful groups, often based on physiological, structural, or functional similarities. This approach is particularly beneficial for complex models characterized by a large number of parameters, whose collective influence can not generally be interpreted in an elementary way with respect to their individual influence on the model.

In this section, groups of parameters (specifically, resistances, inductances and capacitances) related to specific parts of the cardiocirculatory system are considered in order to understand how changes in those groups produce variations in the model's behaviour, in both the systemic and pulmonary circulation cases. Namely, the impact on the simulation of the variation of arterial, venous and capillary parameters is studied; the parameters related to the left ventricle ( $E_{LV}^a$ ,  $E_{LV}^p$  and  $V_{0,LV}$ ) are analyzed to assess how keeping them fixed in the 3D–0D model may limit its ability to accurately reproduce certain hemodynamic conditions (Sections 3.2). The goal is to understand whether fixing these parameters hinders the model from capturing relevant physiological changes, and to what extent this choice influences the simulation outcomes. A noteworthy aspect is the arbitrary choice of groups of parameters; another drawback of the current approach is the fact that other groups of possibly influential parameters may not be considered at all. The sensitivity analysis of these groups of parameters is performed for both ( $\mathcal{C}_{NC}$ ) and ( $\mathcal{C}_{C}$ ); for ( $\mathcal{C}_{C}$ ), the systemic and pulmonary capillary circulation is considered separately.

All the mentioned parameters undergo modification by the multiplication with coefficients in such a way that they are constrained within realistic intervals, while all the others remain unchanged. The modeling of hypertension by means of lumped-parameter models is a topic that has not been systematically exploited yet; different studies employ different models, each with different structures and peculiarities, such as in [51, 52, 53]. Since our sensitivity analysis focuses on the hypertensive setting, constructing realistic parameter intervals is not a trivial task; in this paper, inspiration has been taken from [51, 52, 53] and Section 2, in order to obtain coefficients that would be acceptable and useful for carrying out the sensitivity analysis. These coefficients have been chosen to reflect the typical parameter variations observed during the progression of hypertension: resistances and inductances are

increased while conductances are decreased, and vice versa; active and passive elastance of the left ventricle are enhanced while the resting volume is reduced, and vice versa. Such modifications try to reproduce the haemodynamic alterations reported in clinical and modeling studies, while keeping the parameters within physiologically plausible ranges. The coefficients are defined as follows: The coefficients are defined as follows:

$$\eta_{\rm R} = 1 + 0.15\rho, \qquad \eta_{\rm L} = 1 + 0.075\rho, \qquad \eta_{\rm C} = 1 - 0.06\rho, \qquad (7a)$$

$$\eta_a = 1 + 0.12\rho, \qquad \eta_p = 1 + 0.14\rho, \qquad \eta_0 = 1 - 0.05\rho, \qquad (7b)$$

$$\eta_a = 1 + 0.12\rho, \qquad \eta_p = 1 + 0.14\rho, \qquad \eta_0 = 1 - 0.05\rho, \tag{7b}$$

where  $\eta_R$ ,  $\eta_L$  and  $\eta_C$  are the coefficients applied to resistances, inductances and conductances, respectively;  $\eta_a$ ,  $\eta_p$  and  $\eta_0$  represent the coefficients applied to active elastance, passive elastance and resting volume of left ventricle, respectively; the auxiliary parameter  $\rho$  is defined as  $\rho \in \mathbb{Z} \setminus \{0\}$ , with the constraint  $|\rho| < 5$ .

In this section, to simplify the notation, given a generic parameter or output  $\alpha$  (time dependent or independent), the symbol  $\bar{\alpha}$  will denote the reference value of the parameter or the output computed using the reference parameters, while  $\hat{\alpha}$  will indicate the value of the parameter after being modified according to the guidelines outlined earlier, or the output computed with the modified parameters. Therefore, the following relation holds:  $\hat{\alpha} = \eta_{\alpha}\bar{\alpha}$ , for some parameter  $\alpha$  and the corresponding coefficient  $\eta_{\alpha}$ .

The time-independent outputs monitored in this analysis are listed in C. The variation of an output  $\zeta$  is quantified using the following formula:

$$\Gamma(\zeta) = \left(\frac{\hat{\zeta}}{\bar{\zeta}} - 1\right) \cdot 100. \tag{8}$$

The variables that represent the solutions to the ODE system (Section 3.1) within the simulation are also monitored, along with the pressures in the heart chambers, the fluxes through the cardiac valves and, only for  $(\mathscr{C}_{\mathbb{C}})$ , the non oxygenated pulmonary capillary flux. Since these variables are functions of time (represented as vectors in the numerical solution), four indicators are introduced to simplify the monitoring process and provide scalar values for analysis. They are computed for each variable vas follows:

$$\Gamma_{\mathrm{T}}(v) = \left(\frac{\int_{\mathrm{T-T_{HB}}}^{\mathrm{T}} (\hat{v} - \bar{v}) dt}{\int_{\mathrm{T-T_{HB}}}^{\mathrm{T}} \bar{v} dt}\right) \cdot 100, \quad \bar{\Gamma}(v) = \left(\frac{\mathrm{mean}_t \, \hat{v}}{\mathrm{mean}_t \, \bar{v}} - 1\right) \cdot 100,$$

$$\Gamma_{\mathrm{M}}(v) = \left(\frac{\mathrm{max}_t \, \hat{v}}{\mathrm{max}_t \, \bar{v}} - 1\right) \cdot 100, \qquad \Gamma_{\mathrm{m}}(v) = \left(\frac{\mathrm{min}_t \, \hat{v}}{\mathrm{min}_t \, \bar{v}} - 1\right) \cdot 100.$$
(9)

Additionally, the variation in the PV loops  $\Gamma_i$ , for  $i \in \{LA, LV, RA, RV\}$ , is measured as the ratio between the area of the cycle obtained with modified parameters and the area of the cycle obtained with unmodified parameters.

As the analysis begins, the parameters of a group are modified by means of the coefficients in Equation 7, while all the other parameters remain fixed at reference values. When a simulation is performed, a certain number of time-independent outputs and time-dependent variables are computed: in particular, 45 outputs and 20 variables are computed if ( $\mathscr{C}_{NC}$ ) is employed, while 46 outputs and 25 variables are calculated if  $(\mathscr{C}_{\mathbb{C}})$  is utilized (refer to  $\mathbb{C}$  for the outputs, to Section 3.1 for the variables). Additionally, in the case of  $(\mathscr{C}_{NC})$ , five groups are considered, while seven groups are taken for  $(\mathscr{C}_{C})$ . By using the coefficients in Equation (7), both models' parameters are changed over ten nuances of variation for each considered group: whence, 50 simulations are run for  $(\mathscr{C}_{NC})$  and 70 simulations for (C). For each output, the indicator in Equation (8) is calculated, while, for each variable, the four indicators in Equation (9) are computed; four additional indicators ( $\Gamma_{LA}$ ,  $\Gamma_{LV}$ ,  $\Gamma_{RA}$ ,  $\Gamma_{RV}$ ) are also considered, once for each nuance of variation of each group. All in all, a simulation employing  $(\mathscr{C}_{NC})$  produces 129 indicators and a simulation adopting  $(\mathscr{C}_{C})$  generates 150 indicators, which gives an overall total of 16,950 indicators across all simulations, taking in account every group, every nuance and every model.

At the end of the analysis, the parameters to calibrate comprehend: the active and passive elastances, and the unstressed volume of the four cardiac chambers, the valve maximal and minimal resistances and all the RLC components of the vascular circulation (Section 3.1).

#### 4.2 Implementation of Hypertensive Scenarios

In order to simulate the impact of hypertension in the 0D cardiocirculatory model, it is necessary to introduce systematic modifications of model parameters. Changes in parameters are implemented in such a way that simulated alterations in haemodynamics align with clinical and physiological expectations: this would present a realistic reproduction of hypertensive pathophysiology within the framework of 0D modeling. The modifications are done in the form of percentage changes relative to baseline parameters of a healthy individual, collected in B: all those adjustments try to represent the physiological processes explained in Section 2, maintaining a consistent representation of hypertensive condition. The result obtained from sensitivity analysis (Section 4.1) are supporting guidelines to enhance the modifications, helping to achieve the desired haemodynamic effects within the model.

In this study, three distinct types of hypertension are considered (Section 2.1), each characterized by different haemodynamic implications and clinical relevance:

- 1. systemic hypertension, mostly affecting the systemic arterial circulation and commonly associated with increased peripheral resistance;
- 2. pulmonary hypertension, involving elevated pressure in the pulmonary circulation;
- 3. renovascular hypertension, due to abnormalities in kidneys, which gives rise to compensatory mechanisms, further increasing systemic blood pressure; the examined condition is also aggravated by secondary pulmonary hypertension.

For each of these conditions, three different levels of severity (mild, moderate and severe) are investigated, in an effort to capture the progressive nature of the disease and its effects on the circulatory dynamics; the choice of these three levels of severity was made in such a way as to represent the range of hypertensive conditions that might be observed in a realistic patient population. The parameter changes are listed in Table 1, indicating the parameter adjustments for each condition and severity level.

#### 4.3 Models Calibration

In this section, two different calibration procedures for the 0D and the 3D–0D models are presented, respectively in Sections 4.3.1 and 4.3.2; since the models are profoundly different also in terms of the computational cost required to solve them, it was deemed appropriate to adopt two different calibration strategies.

#### 4.3.1 Calibration of the 0D model

The calibration procedure that is presented in this section follows the framework described in [31], which, in turn, relies on the method presented in [54]. The process begins by defining a loss function that quantifies the discrepancy between simulation results and target values. The aim of calibration is identifying the parameter configuration  $\bar{\mathbf{p}}^j \in \Theta = \mathbb{R}^{N_p}$ , with  $N_p$  being the number of parameters to calibrate, that minimizes the loss function; in order to find the configuration  $\bar{\mathbf{p}}^j$ , parameters are iteratively modified within predefined bounds, untill the loss function is sufficiently small. In [31], the loss function is given by the sum of squared relative errors between model outputs and target data, for the specific individual j, as follows:

$$\bar{\mathbf{p}}^j = \underset{\mathbf{p} \in \Theta}{\operatorname{arg\,min}} \ \mathcal{L}^j(\mathbf{p}),\tag{10}$$

with the relative error  $\delta_k^j$  and the loss function  $\mathcal{L}^j$ , defined as:

$$\delta_k^j(\mathbf{p}) = \left| \frac{q_{\mathbf{m}_j(k)}(\mathbf{p}) - d_k^j}{d_k^j} \right|, \qquad \mathcal{L}^j(\mathbf{p}) = \sum_{k=1}^{N_j} \delta_k^j(\mathbf{p})^2, \tag{11}$$

		Systemic			Pulmonary	7		Renovascula	ar
Parameter	Mild	Moderate	Severe	Mild	Moderate	Severe	Mild	Moderate	Severe
HR	_	+5%	+10%	_	+5%	+10%	_	_	+10%
$\mathrm{E}_{\mathrm{LV}}^a$	+10%	+20%	+40%	+5%	+10%	+15%	_	_	_
$ m V_{0,LV}$	_	_	-10%	_	_	-10%	_	_	_
$ m R_{AR}^{SYS}$	+10%	+30%	+50%	_	_	+5%	+15%	+40%	+85%
$\mathrm{C_{AR}^{SYS}}$	-10%	-20%	-40%	_	_	-10%	-10%	-15%	-25%
$ m R_{VEN}^{SYS}$	_	_	+5%	_	_	_	_	_	_
$\mathrm{C_{VEN}^{SYS}}$	_	_	-5%	_	_	_	_	_	_
$ m R_{AR}^{PUL}$	_	_	+10%	+20%	+50%	+100%	+5%	+15%	+40%
$\mathrm{C_{AR}^{PUL}}$	_	_	-10%	-10%	-25%	-50%	_	_	_
$ m R_{VEN}^{PUL}$	_	_	_	+10%	+25%	+50%	_	_	_
$\mathrm{C_{VEN}^{PUL}}$	_	_	_	-10%	-25%	-50%	_	_	_
$ m R_{C}^{SYS}$	_	_	+10%	_	_	_	_	_	_
$\mathrm{C}_{\mathrm{C}}^{\mathrm{SYS}}$	_	_	-20%	_	_	_	_	_	_
$ m R_{C}^{PUL}$	_	_	_	+10%	+30%	+60%	+5%	+10%	+25%
$\mathrm{C}_{\mathrm{C}}^{\mathrm{PUL}}$	_	_	_	_	_	-20%	_	_	_
$R_{ m AV}$	+25%	+50%	+100%	_	_	_	+25%	+50%	+100%
$R_{ m MV}$	_	+10%	+20%	_	_	_	+10%	+20%	+30%
$R_{ m PV}$	_	_	_	+25%	+50%	+100%	+25%	+50%	+100%
$R_{\mathrm{TV}}$	_	_	_	+10%	+25%	+50%	+10%	+25%	+50%

Table 1: Modifications applied to the model parameters to simulate mild, moderate and severe hypertension. The changes are expressed as percentage variations relative to the baseline parameters of a healthy individual, which are reported in B.

where  $N_j$  is the number of available data for individual j,  $d_k^j$  represents the k-th target data value of individual j, and  $q_{m_j(k)}^j(\mathbf{p})$  is the corresponding model output. The index m for  $q_m^j$  is  $m \in \{1, \ldots, N_q\}$ , where  $N_q$  is the total number of distinct model outputs. For more details about parameters  $\mathbf{p}$  to be calibrated, refer to Section 4.1.

To minimize  $\mathcal{L}^j$ , parameters are optimized within predefined intervals  $I_i$ , where  $i \in \{1, \dots, N_p\}$ . These intervals are set around some initial reference values in such a way that, after the optimization, the changes in parameters remain physically and clinically relevant. The value of the loss function falling below some given small threshold, set to  $10^{-3}$ , is assumed to indicate a successful calibration. Nevertheless, there are cases where the procedure might be unsuccessful, such as when the loss function's minimum is located above the threshold, meaning the parameter set is not able to reproduce the reference data within the given constraints. The minimization of  $\mathcal{L}^j$  is performed in Python using the Quasi-Newton optimization algorithm L-BFGS-B [55], as implemented in the SciPy library [56].

An Alternative Choice for the Loss Function. Apart from the choice of an optimization algorithm, another important issue in model calibration is related to the selection of a suitable loss function, which drives the optimization procedure. The selection or design of an appropriate loss function is particularly critical in the context of cardiocirculatory models, where complex physiological dynamics must be captured with high fidelity during the calibration process. The method is based on constructing alternative loss functions that apply distinct penalizations to different magnitudes of parameter values; subsequently, these various loss functions are applied for the calibration process so that the results of the estimated parameters and the associated calibration performance could be compared. Since the following analysis does not focus on the individual from whom the data is provided but rather the functional form of the loss function, the index j in Equations (10) and (11) will be

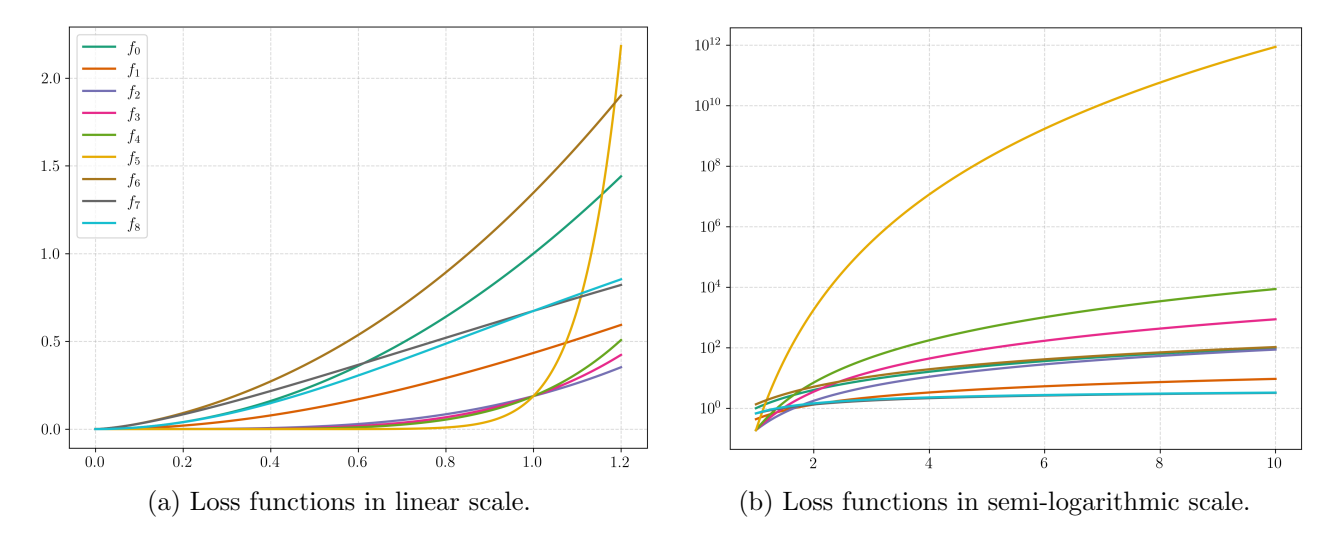


Figure 3: Comparison of the eight loss functions used in this study: on the left, they are represented in linear scale for  $\delta \in [0, 1.2]$ , while on the right in semi-logarithmic scale on y axis for  $\delta \in [1, 10]$ .

omitted to simplify the notation; additionally, the index r and the total parameter deviation  $\Delta_r$  are introduced as follows:

$$\mathcal{L}_r(\mathbf{p}) = \sum_{k=1}^{N} f_r(\delta_k(\mathbf{p})), \qquad \Delta_r(\mathbf{p}) = \sum_{k=1}^{N} \delta_k(\mathbf{p}), \qquad (12a)$$

such that  $f_r$  denotes a different function as r changes in the subsequent analysis. By defining the following functions:

$$f_0(\delta) = \delta^2,$$
  $g(\delta) = \log(\cosh \delta),$   $h(\delta) = 1 + \frac{1}{2}\log(1 + \delta^2),$ 

it is possible to express the different functions  $f_r$  besides  $f_0$  (Figure 3), chosen to be subsequently analyzed, as follows:

$$f_1(\delta) = g(\delta),$$
  $f_2(\delta) = g(\delta)^2,$   $f_3(\delta) = |\delta| g(\delta)^2,$   $f_4(\delta) = \delta^2 g(\delta)^2,$   $f_5(\delta) = \delta^{10} g(\delta)^2,$  (13a)

$$f_6(\delta) = |\delta|^{\frac{3}{2}} h(\delta), \quad f_7(\delta) = \frac{|\delta|^{\frac{3}{2}}}{1 + |\delta|^{\frac{3}{2}}} h(\delta), \quad f_8(\delta) = \frac{\delta^2}{1 + \delta^2} h(\delta).$$
 (13b)

To investigate the impact of the different choices of  $f_r$  in the loss function definition in Equation (12), a systematic study has been conducted. In the absence of real clinical data, a synthetic approach is adopted: data from a healthy individual (B) are used as a baseline, and modifications are introduced to replicate the causes and effects of hypertension. These modified datasets are employed as input for simulations performed using the ( $\mathcal{C}_{\rm C}$ ) model, that has been discussed in Section 3.1; time-independent outputs from these simulations are then collected to serve as reference data. The next step involves calibrating ( $\mathcal{C}_{\rm NC}$ ), presented in Section 3.1, using these time-independent outputs as targets: for the selection of the outputs utilized in the calibration process, all the outputs included in C are considered. As for the parameters to be calibrated, reference is made to the total Sobol indices  $\mathcal{S}^{\mathcal{T}}$  presented in Figure 2: specifically, only those parameters  $p_k$  such that  $\exists j: \mathcal{S}_k^{j,\mathcal{T}} \geq 0.2$  are selected for calibration.

This setup is intentionally designed to enable a focused comparison of different loss functions, without introducing additional variability related to capillary dynamics in the model being calibrated. Using  $(\mathscr{C}_{C})$  to generate the reference data and calibrating  $(\mathscr{C}_{NC})$  ensures that the evaluation of the loss functions is not influenced by the added complexity of capillary parameters. Moreover,  $(\mathscr{C}_{C})$  is

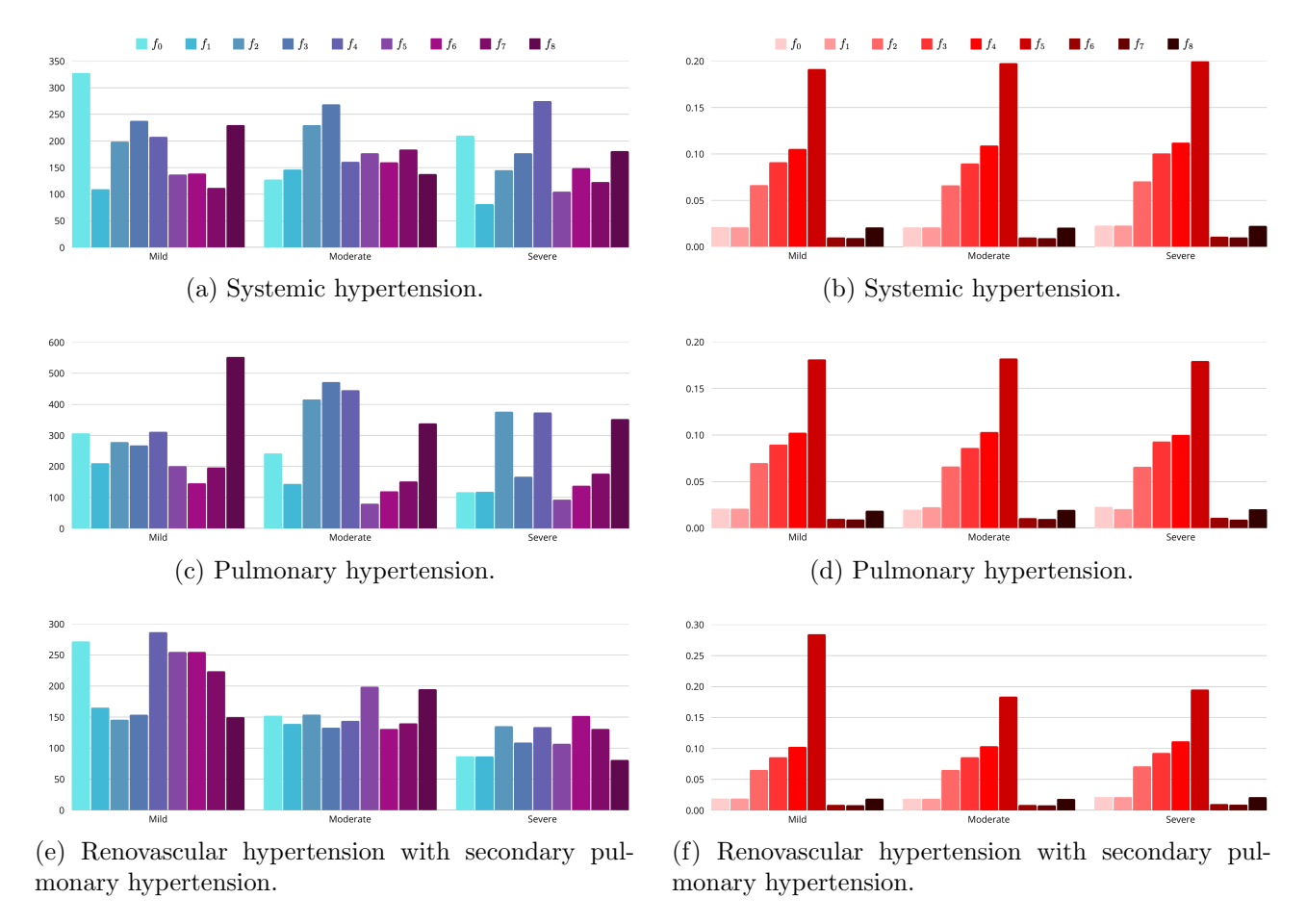


Figure 4: Calibration times (in seconds, on the left) and total parameter deviations  $\Delta_r$  (on the right) at the end of calibration for ( $\mathcal{C}_{NC}$ ). The following conditions are studied: systemic, pulmonary and renovascular hypertension with secondary pulmonary hypertension. Three severity levels (mild, moderate and severe) are considered for each condition, and the calibration is performed using different choices for the loss function.

not calibrated anywhere in this study, both because the calibration procedure is more challenging and because it tends to produce parameter values that result in less physiologically realistic cardiac and circulatory dynamics compared to those obtained with  $(\mathscr{C}_{NC})$ .

For each candidate loss function in Equation (13), the calibration process is carried out to determine the optimal parameter configuration, and the time needed is recorded; then, the vectorial outputs from the two models as in D are compared. This procedure is repeated for the cases presented in Section 4.2, encompassing systemic hypertension, pulmonary hypertension and renovascular hypertension with secondary pulmonary hypertension. Each of these conditions is further studied at three different levels of gravity (mild, moderate and severe hypertension), allowing a thorough check of the loss functions in a wide variety of situations. The whole analysis has been performed on a MacBook Pro (Apple M1 Pro, 10 cores, 3.2 GHz, 16 GB RAM). Times necessary to complete the calibration for each analyzed case with a different choice of the loss function are summarized in Figure 4. Among all the candidate functions,  $f_1$  stands out as the optimal selection: even if the total parameter deviations in Figure 4 are generally smaller for  $f_6$  and  $f_7$ ,  $f_1$  requires the shortest calibration time, being the best compromise between quality of the parameters and calibration time. As a result of this analysis, all subsequent calibrations are performed using  $f_1$  as the function defining the loss; for simplicity, from this point onward, the loss function will be denoted as  $\mathcal{L}$  in place of  $\mathcal{L}_1$ .

#### 4.3.2 Calibration of the 3D-0D model

In general, the calibration of a 3D–0D model is computationally expensive, due to the high complexity of the three-dimensional representation of the left ventricle, making both single-parameter and

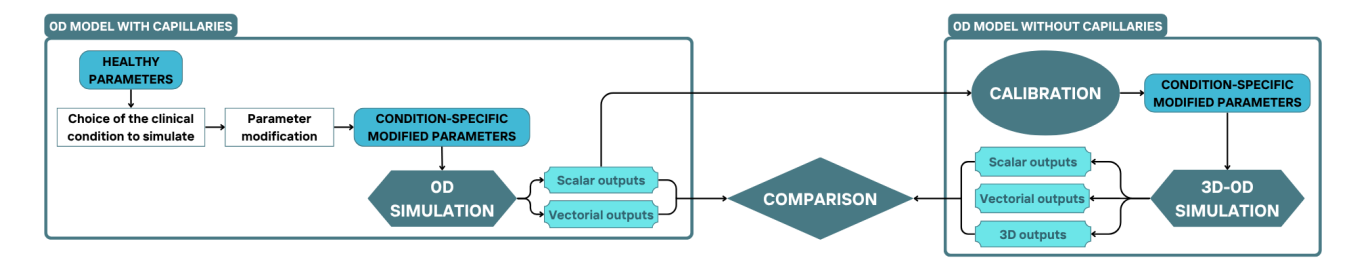


Figure 5: Workflow illustrating the calibration process of 3D–0D models for a generic clinical scenario.

multi-parameter sensitivity analysis unfeasible. Even a direct calibration would be impractical, as it would require, among other things, solving the 3D–0D model many times, an operation that is computationally expensive. In addition, a whole calibration process would be required for each case of hypertension that is to be analysed, nine in total (Section 4.2), making the approach even less feasible; lastly, all the adjustments performed to simulate hypertension involve only parameters of the 0D circulation model (as detailed in Section 4.2). In light of all these considerations, an alternative and more computationally efficient approach, depicted in Figure 5, is preferred.

The workflow starts by exploiting the 0D model with capillary circulation, ( $\mathscr{C}_{C}$ ), which allows a direct manipulation on parameters related to capillaries: through modification of ( $\mathscr{C}_{C}$ ), a direct action is exerted on the capillary circulation in order to ensure that, after the calibration of the electrome-chanical model, the 3D–0D representation also reflects the effects of hypertension at the capillary level, despite capillaries are not physically included in the 3D–0D model. Taking the parameters of a healthy individual (B), the adjustments to simulate hypertension, as outlined in Section 4.2, are then applied to this model. A simulation is performed, and its time-independent outputs are used to calibrate, following the procedure illustrated in Section 4.3.1, a 0D model without capillary circulation, ( $\mathscr{C}_{NC}$ ): such a procedure allows for direct manipulations of the capillary network and ensures that ( $\mathscr{C}_{NC}$ ) properly captures the effects produced by these manipulations.

It is important to remark here that all the parameters related to the left ventricle, which are active and passive elastance and the unstressed volume, are not included in this calibration procedure: such a choice is indeed motivated by the fact that, in the 3D–0D framework, the left ventricle is represented by means of a 3D electromechanical structure, as described in Section 3.2, which is inherently not including these latter parameters; the mesh employed in the 3D–0D model is generated from the left ventricle of a healthy individual, as explained in Section 3.2. It would hence be inconsistent to modify the 0D left ventricle parameters because changes in such parameters can not be replicated in the 3D electromechanical model. For additional information, refer to the details about the left ventricle, in Chapter 2, and Sections 4.1 and 4.2.

As illustrated in Figure 5, the parameters of  $(\mathscr{C}_{NC})$  are calibrated, using the time-independent outputs of  $(\mathscr{C}_{C})$ , and then included in the 3D–0D model. It is noteworthy that the parameters of the 3D–0D model related to the electromechanical component of the left ventricle are never modified: as they are very delicate quantities and closely linked to the specific model itself, it would be unfeasible to try to adapt them to simulate hypertension. For this reason, the same parameters defined in [29] are employed. Finally, a simulation is performed under this comprehensive framework, allowing for the analysis of the model's behaviour under hypertensive conditions. The results obtained from  $(\mathscr{C}_{C})$  and from the 3D–0D model are then compared to check if the calibration is performed successfully: by effectively aligning the outputs of  $(\mathscr{C}_{C})$  and the 3D–0D model, the latter is now able to give real insight into the complex dynamics of hypertension, achieving this goal with minimal computational effort.

This calibration workflow also lays the foundation for cardiovascular DTs. By aligning the outputs of the 0D and 3D–0D models, it becomes possible to generate patient-specific representations of cardiac dynamics under hypertensive conditions. Such personalized models could be further exploited for predictive simulations, risk assessment and clinical monitoring, highlighting the potential of DTs in supporting individualized diagnosis and therapy planning.

			0D model				3D-0	D model	
Output	Unit	Healthy	Mild	Moderate	Severe	Healthy	Mild	Moderate	Severe
$\overline{ m LV_{SW}}$	$mmHg \cdot L$	5.9	6.3	6.9	7.5	6.3	6.5	7.1	7.2
CI	$\mathrm{m}^2\cdot\mathrm{L/min}$	2.9	2.9	3.0	3.0	3.0	3.0	3.0	3.1
$SAP_{max}$	mmHg	109.6	117.0	128.2	144.4	106.9	111.4	120.9	127.4
$SAP_{min}$	mmHg	71.2	74.5	80.2	83.8	72.8	76.5	81.5	80.8

Table 2: Variations of selected time-independent outputs in systemic hypertension, from both ( $\mathscr{C}_{C}$ ) and 3D–0D model.

#### 5 Numerical Results and Discussion

Each simulation generates a total of 25 time-dependent variables and 46 outputs, if carried out with  $(\mathcal{C}_{\rm C})$ , or 20 time-dependent variables and 45 outputs, if the 3D–0D model is employed (Section 3.1 for further details); in addition, the 3D–0D model calculates key quantities from the electromechanical model (Section 3.2), of the left ventricle mesh. For both 0D and 3D–0D models, right and left ventricular stroke work (respectively, RV<sub>SW</sub> and LV<sub>SW</sub>) is computed as the area enclosed within the corresponding PV loop. Stroke work was not used for parameter calibration because it showed low sensitivity to model parameters, making it less informative for optimization purposes. Moreover, the information it provides is largely redundant with that already captured by the pressure and volume curves, which are directly included in the loss function. Although these quantities are not directly used for parameter calibration, they provide valuable insight into ventricular function.

Each condition is simulated through parameter adjustment, as outlined in Section 4.2; the timestep employed in 0D simulation is  $10^{-3}$  s, whereas a more restrictive value of  $10^{-4}$  s is preferred for the 3D–0D model to account for the fast time scale charachtering electrophysiology. The calibration process for ( $\mathcal{C}_{\rm C}$ ) is performed as described in Section 4.3.1, while the calibration for the 3D–0D model is carried out as outlined in Section 4.3.2. As mentioned in Section 4.3.2, in order to ensure consistency in the calibration process, the left ventricle parameters remain unchanged in the 3D–0D model, since the left ventricle mesh is constructed on the basis of a healthy individual: from a clinical point of view, this fact may be interpreted as a representation of an individual with a hypertensive condition, which might also be very severe, but not of long-standing duration, i.e. the high pressure has not yet seriously compromised the left ventricular structure. It is worth noting that the results presented in the following sections also illustrate the potential of the calibrated models to serve as the foundation for patient-specific cardiovascular DTs, enabling personalized insights and predictive analyses.

#### 5.1 Systemic Hypertension

Starting from  $p_{\rm LV}$ , in Figures 6a and 6c ( $C_{\rm C}$ ) shows a marked increase in peak and end-systolic values, reflecting the increased afterload that forces the ventricle to generate higher pressures. The 3D–0D model confirms this trend but also reproduces a more realistic pressure curve, closer to patient data, with the distinct behaviors of pressure in the different phases more clearly visible, together with an increase in both  $p_{\rm LV}$  and  $V_{\rm LV}$  in Figures 6b and 6d: this leads to a more consistent description of ventricular mechanics in hypertensive conditions [23]. As shown in Table 2, the effect on LV<sub>SW</sub> is evident in both models, with a progressive raise as vascular resistance increases. In the 0D case, this increase represents the ventricle's attempt to compensate for the increase in afterload, even though it proves insufficient to sustain adequate flow. The 3D–0D model also predicts a higher LV<sub>SW</sub>, but with a pressure-volume evolution that better matches clinical expectations, as the loop shows an upward shift in the minimal and maximal pressure, thus providing a more accurate picture of the increase in workload [57]. Considering  $Q_{\rm AV}$  in Figures 6e and 6f, both models show a reduction with disease progression, due to compromised filling and limited ejection, with the 3D–0D model displaying more realistic peak values [58], due to the more accurate simulation of systolic ejection dynamics by the 3D ventricle

As shown in Table 2, CI shows opposite trends in the two models: in  $(\mathscr{C}_{\mathbb{C}})$ , it appears to increase

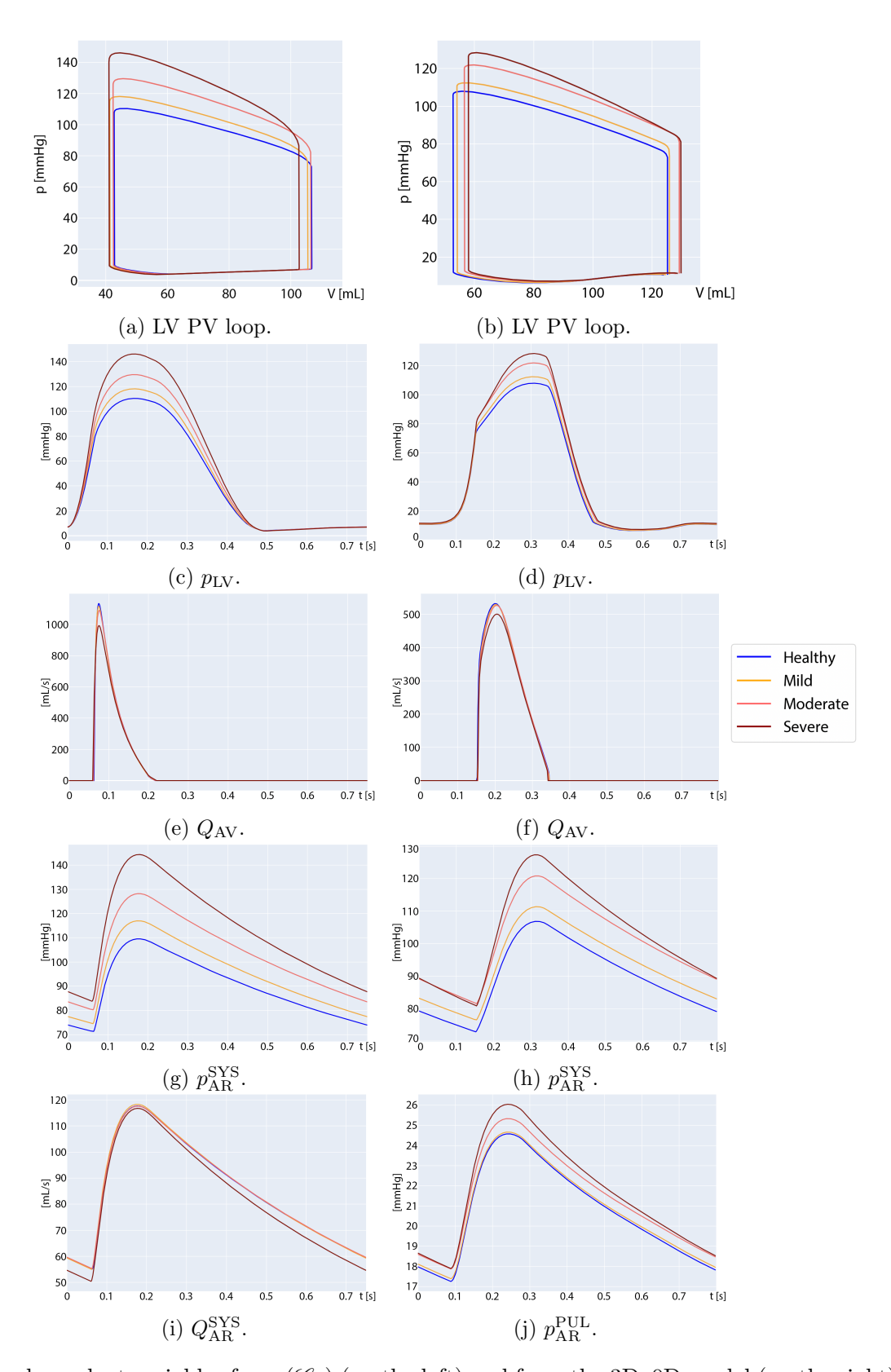


Figure 6: Time-dependent variables from  $(\mathscr{C}_{\mathbb{C}})$  (on the left) and from the 3D–0D model (on the right). Mild, moderate and severe systemic hypertension (in orange, light red and dark red) is compared with a healthy individual (in blue).

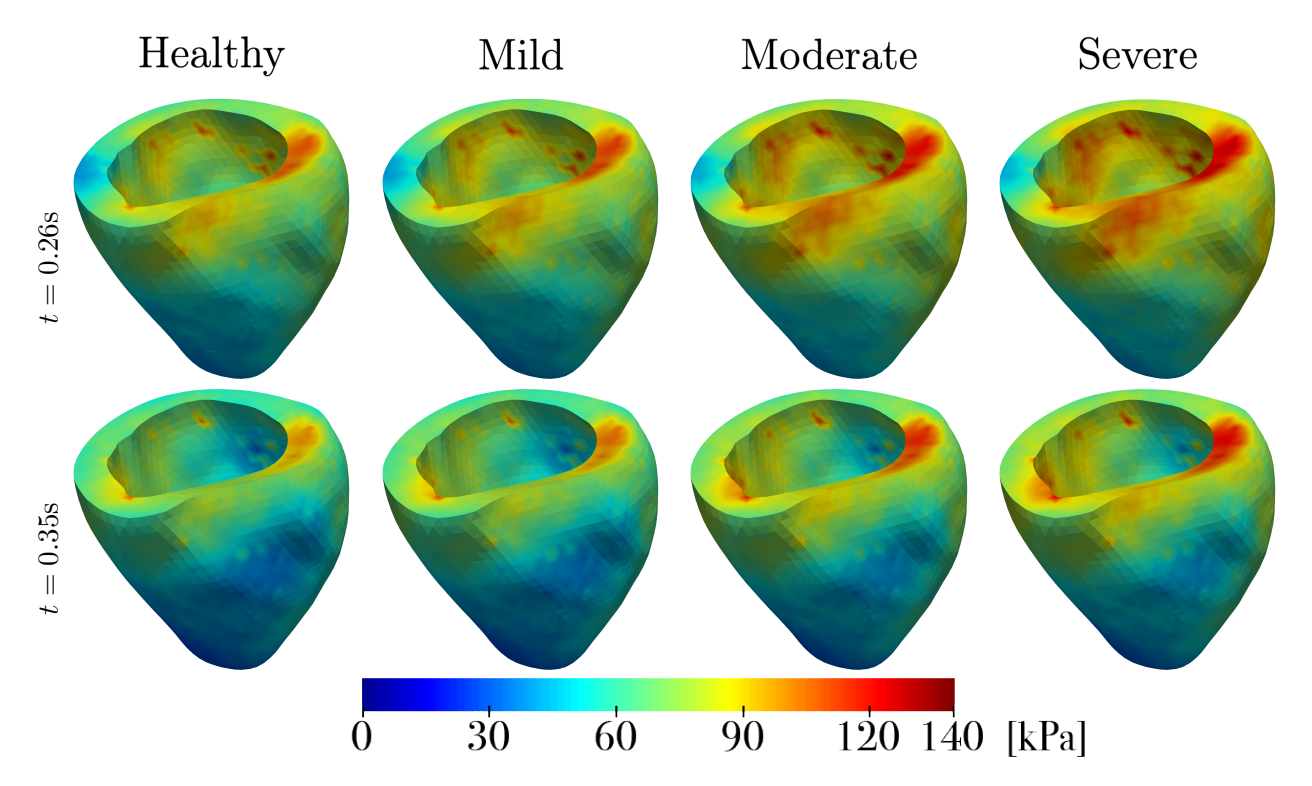


Figure 7: Evolution of the active tension  $T_a$  in the left ventricle during the last cardiac cycle. Each picture is displayed on the reference configuration  $\Omega_0$ . Mild, moderate and severe systemic hypertension is compared with a healthy individual.

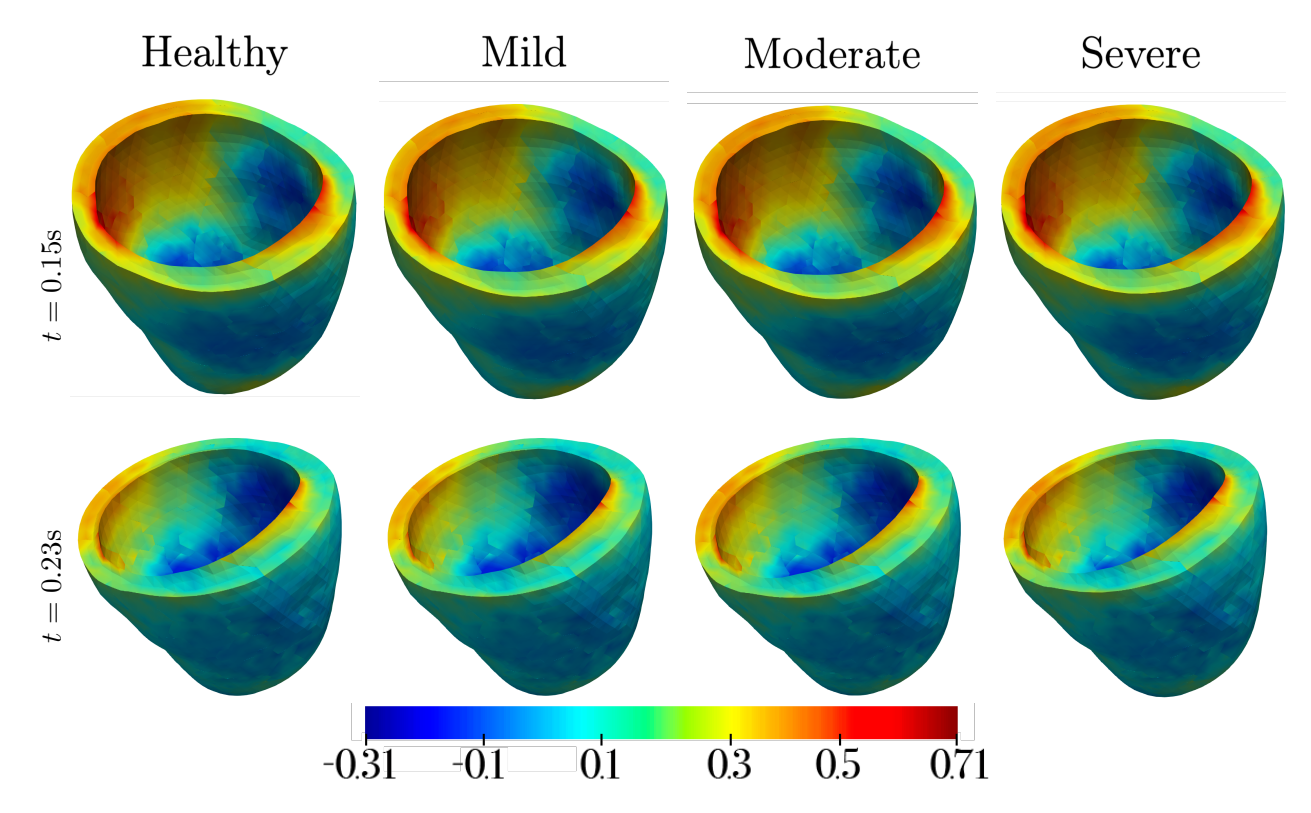


Figure 8: Evolution of the Green-Lagrange strain trace  $tr(\mathbf{E})$  in the left ventricle during the last cardiac cycle. Each picture is warped by the displacement vector  $\mathbf{d}$ . Mild, moderate and severe systemic hypertension is compared with a healthy individual.

slightly, mainly due to the greater pressure generation by the ventricle; however, this result is not consistent with clinical evidence [59]. The 3D–0D model avoids this artefact, showing a more stable CI, which is more in line with the haemodynamic response expected in systemic hypertension [59].

		0D model				3D-0	D model		
Output	Unit	Healthy	Mild	Moderate	Severe	Healthy	Mild	Moderate	Severe
$\overline{ m RV}_{ m IEDV}$	$\mathrm{mL/m^2}$	68.2	70.3	73.4	78.1	71.5	73.6	78.6	86.0
$\mathrm{RV}_{\mathrm{IESV}}$	$\mathrm{mL/m^2}$	32.6	35.0	38.7	44.8	34.2	36.2	40.2	46.9
$\mathrm{RV}_{\mathrm{EF}}$	%	52.2	50.2	47.3	42.6	52.2	50.9	48.9	45.5
$\mathrm{RV}_\mathrm{SW}$	$mmHg \cdot L$	1.2	1.3	1.5	1.6	1.5	1.6	1.8	2.0
$\max \nabla p_{\mathrm{rAV}}$	mmHg	17.3	19.6	22.6	27.6	26.4	28.4	31.0	35.1

Table 3: Variations of selected time-independent outputs in pulmonary hypertension, from both ( $\mathscr{C}_{C}$ ) and 3D–0D model.

Focusing on  $p_{\rm AR}^{\rm SYS}$  in Figures 6g and 6h, both models capture the increase in systolic and diastolic values. In  $(\mathcal{C}_{\rm C})$ , this is reflected in an increase in SAP<sub>max</sub> and SAP<sub>min</sub> (Table 2), indicative of the heavier load imposed on the heart; the 3D–0D model confirms these trends, but with a slightly lower systolic peak. Quantitatively, SAP<sub>max</sub> increases steadily, while SAP<sub>min</sub> increases more moderately before showing a slight decrease in the most severe phase (Table 2). With regard to  $Q_{\rm AR}^{\rm SYS}$  in Figure 6i,  $(\mathcal{C}_{\rm C})$  suggests initial stability followed by a decline, which could lead to a reduction in peripheral perfusion. Furthermore, in Figure 6j the 3D–0D model shows that  $p_{\rm AR}^{\rm PUL}$  remains nearly unchanged in mild severity, consistently with clinical evidence indicating that systemic hypertension primarily affects the systemic circulation, with pulmonary pressures increasing only in advanced stages due to backward transmission, i.e. the rise in left heart pressures being passively transmitted to the pulmonary vessels.

Finally, active tension in Figure 7 shows a notable peak increase during isovolumetric contraction and ejection, reflecting the need for higher contractile force to counteract the increased afterload; in addition, spatially resolved active tension peaks in the top portion of the left ventricle at t = 0.26 s and t = 0.35 s, suggesting regional stress, potentially due to local hypertrophy or contractile heterogeneity [60]. The trace of the Green-Lagrange strain tensor  $\mathbf{E} = \frac{1}{2}(\mathbf{C} - \mathbf{I})$  in Figure 8 shows only minor changes, with a slight increase in  $|\text{tr}(\mathbf{E})|$  maximal values. This indicates a marginal increase in ventricular dilation and a slightly stronger contraction during the cardiac cycle, consistent with the higher arterial pressure. The overall volumetric deformation remains close to the physiological case.

#### 5.2 Pulmonary Hypertension

Considering the right ventricular PV loop in Figures 9a and 9b, both end-systolic and end-diastolic pressures increase in  $(\mathcal{C}_C)$ , and the ventricle becomes stiffer. The 3D–0D loop shows a similar overall trend, but the 3D representation allows for a more physiologically accurate description of ejection dynamics and regional mechanics [61].

Looking at right ventricular volumes, as shown in Table 3, both models detect a marked increase in  $RV_{IEDV}$ , reflecting higher filling pressures and ventricular dilatation. In ( $\mathcal{C}_{C}$ ),  $RV_{IESV}$  also increases, leading to a reduction in  $RV_{EF}$  and impaired  $Q_{PV}$  in Figure 9c. The 3D–0D model confirms the increase in  $RV_{IESV}$  and the decrease in  $RV_{EF}$ , highlighting the progressive inefficiency of right ventricular emptying. In particular, unlike the 0D model,  $Q_{PV}$  remains relatively stable in the 3D–0D case (Figure 9d), suggesting that the right ventricle compensates through increased pressure generation to preserve stroke volume despite increased resistance.

As shown in Table 3, RV<sub>SW</sub> increases in both models, reflecting the increased energy demand imposed by pulmonary hypertension. While ( $\mathcal{C}_{\rm C}$ ) quantifies this increase as a compensatory response to maintain flow, the 3D–0D model integrates this increase with the spatial distribution of ventricular contraction, providing a more realistic assessment of workload [62].  $p_{\rm AR}^{\rm PUL}$  increases in both models (Figures 9e and 9f), demonstrating the afterload imposed on the right ventricle;  $Q_{\rm AR}^{\rm PUL}$  decreases in 0D due to limited ventricular ejection (Figure 9g), whereas in the 3D–0D model, the flow curve is flatter and more prolonged, reflecting a delayed peak and a more physiological right ventricular ejection under pulmonary hypertension. [63] (Figure 9h). In Figures 9i and 9j,  $Q_{\rm VEN}^{\rm SYS}$  is compromised in the 0D model, potentially causing congestion, while in 3D–0D it increases as a compensatory mechanism to attenuate pressure variations, although this may ultimately fail in cases of further aggravated

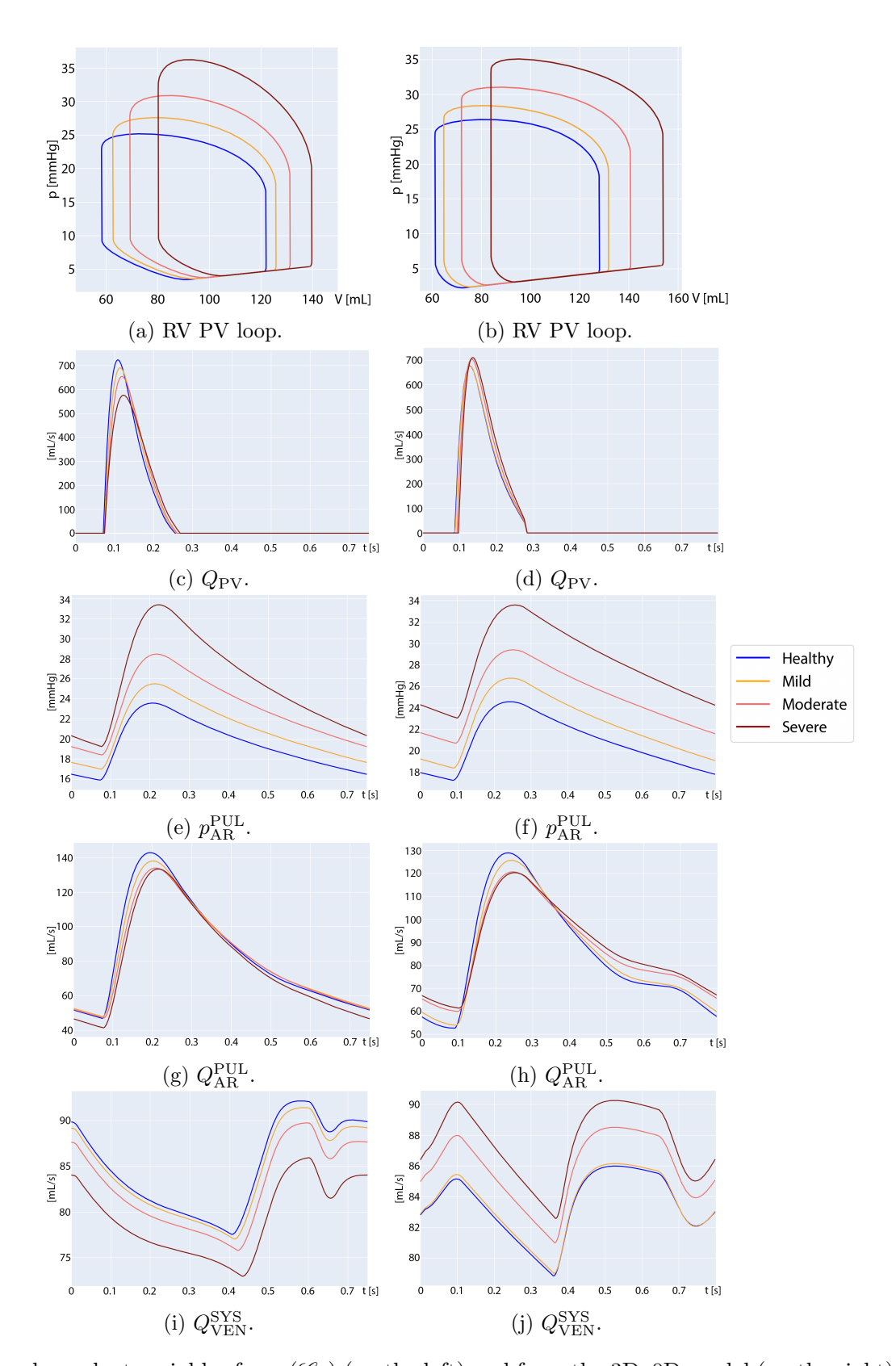


Figure 9: Time-dependent variables from  $(\mathcal{C}_C)$  (on the left) and from the 3D–0D model (on the right). Mild, moderate and severe pulmonary hypertension (in orange, light red and dark red) is compared with a healthy individual (in blue).

			0D model			3D–0D model			
Output	Unit	Healthy	Mild	Moderate	Severe	Healthy	Mild	Moderate	Severe
$\overline{ m LV_{IEDV}}$	$\mathrm{mL/m^2}$	59.7	61.6	69.0	79.6	69.9	71.4	75.4	82.3
$LV_{IESV}$	$\mathrm{mL/m^2}$	23.9	25.8	30.7	38.7	29.5	31.0	32.8	34.4
$\mathrm{RV}_{\mathrm{IEDV}}$	$\mathrm{mL/m^2}$	68.2	69.0	75.3	83.7	71.5	72.4	79.7	93.8
$\mathrm{RV}_{\mathrm{IESV}}$	$mL/m^2$	32.6	33.5	37.2	43.2	34.2	34.8	38.5	45.2
$\mathrm{LV}_{\mathrm{SW}}$	$\mathrm{mmHg}\cdot\mathrm{L}$	5.9	6.4	8.4	11.6	6.3	6.8	7.8	9.5
$\mathrm{RV}_\mathrm{SW}$	$mmHg \cdot L$	1.1	1.3	1.6	2.1	1.5	1.5	1.9	2.7

Table 4: Variations of selected time-independent outputs in renovascular hypertension with secondary pulmonary hypertension, from both ( $\mathscr{C}_{\mathcal{C}}$ ) and 3D–0D model.

conditions. Finally,  $\max \nabla p_{\text{rAV}}$  rises in both models (Table 3), reflecting reduced filling efficiency and reduced overall cardiac performance. Interventricular interactions may further compromise left ventricular filling, an effect present in 0D and less pronounced in 3D–0D due to more accurate spatial resolution.

As pulmonary hypertension mainly affects right ventricular dynamics, only marginal effects are expected on the left ventricle in the absence of left-sided dysfunction [17, 63]; then, no figures related to 3D left ventricular variables are included.

#### 5.3 Renovascular Hypertension with Secondary Pulmonary Hypertension

In both models, the left ventricular PV loop (Figures 10a and 10b) shows a clear increase in end-systolic pressure due to high systemic vascular resistance, leading to an increase in LV<sub>SW</sub> (Table 4); however, in the 3D–0D model, systolic work is slightly lower in severe hypertension, suggesting a more physiologically realistic redistribution of workload, likely due to the spatial heterogeneity of myocardial contraction captured by the 3D mechanics. As presented in Table 4, LV<sub>IEDV</sub> increases progressively in both models, but the 3D–0D predictions are slightly higher than ( $\mathcal{C}_{\rm C}$ ), indicating more pronounced ventricular dilatation; LV<sub>IESV</sub> also increases in both models, but the 3D–0D increase is more moderate, reflecting relatively preserved systolic emptying compared to the 0D results.

The right ventricle responds to secondary pulmonary hypertension with elevated end-diastolic and end-systolic volumes in both models, as shown by  $RV_{IEDV}$  and  $RV_{IESV}$  in Table 4, and by the right ventricular PV loops in Figures 10c and 10d. The 3D–0D model generally predicts slightly higher values, in line with increased filling in the presence of higher afterload.  $RV_{SW}$  and  $RV_{IESV}$  increase in both models, with the 3D–0D simulation showing slightly higher values, reflecting the greater energy demand and ventricular filling under increased pulmonary resistance.

Both  $p_{\rm AR}^{\rm SYS}$  (Figures 10e and 10f) and  $Q_{\rm AR}^{\rm SYS}$  (Figures 10g and 10h) increase in both models, as the circulation adapts to preserve systemic perfusion. In ( $\mathcal{C}_{\rm C}$ ), these increases appear more uniform throughout the entire cardiac cycle, while in the 3D–0D model they are more concentrated around the systolic peak: this difference originates from the more detailed spatial representation of the left ventricle in the 3D–0D framework, which captures the non-linear interplay between ventricular contraction, pressure wave propagation and vascular impedance. As a result, the 3D–0D model provides a sharper and more realistic distribution of pressures and flows, whereas ( $\mathcal{C}_{\rm C}$ ), due to its lumped nature, tends to smooth out temporal variations and therefore depicts a more averaged behaviour. In Figures 10i and 10j,  $p_{\rm AR}^{\rm PUL}$  also increases due to secondary pulmonary hypertension, while the 3D–0D model highlights how the right ventricle buffers left ventricular preload, maintaining higher volumes and systolic work and capturing ventriculo-vascular interactions more accurately than the 0D simulation. In Figure 11, raised  $p_{\rm C}^{\rm PUL}$  and  $Q_{\rm C}^{\rm PUL}$  suggest altered lung microcirculation in the 0D representation, risking fluid buildup and impaired gas exchange, while increased  $p_{\rm C}^{\rm SYS}$  point to systemic microvascular dysfunction, leading to tissue oedema and impaired nutrient delivery [64].

In Figure 12, active tension markedly increases in maximal mean values, enhancing pumping during ejection; maximal and minimal values rise over the entire left ventricle, with the upper ventricle showing the greatest increase at  $t = 0.26 \,\mathrm{s}$  and  $t = 0.35 \,\mathrm{s}$ . The trace of **E** in Figure 13 exhibits more

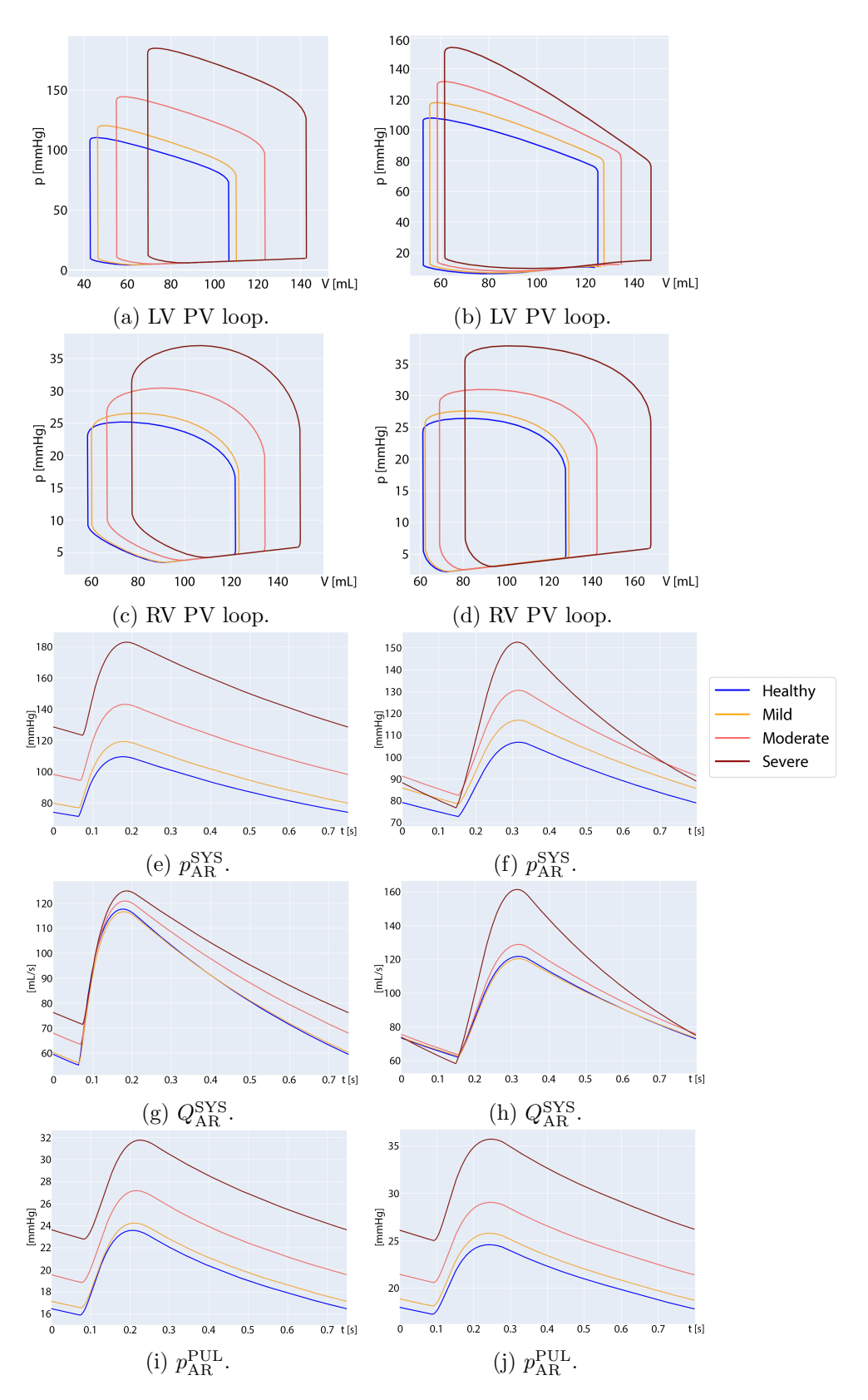


Figure 10: Time-dependent variables from  $(\mathcal{C}_C)$  (on the left) and from the 3D–0D model (on the right). Mild, moderate and severe renovascular hypertension with secondary pulmonary hypertension (in orange, light red and dark red) is compared with a healthy individual (in blue).

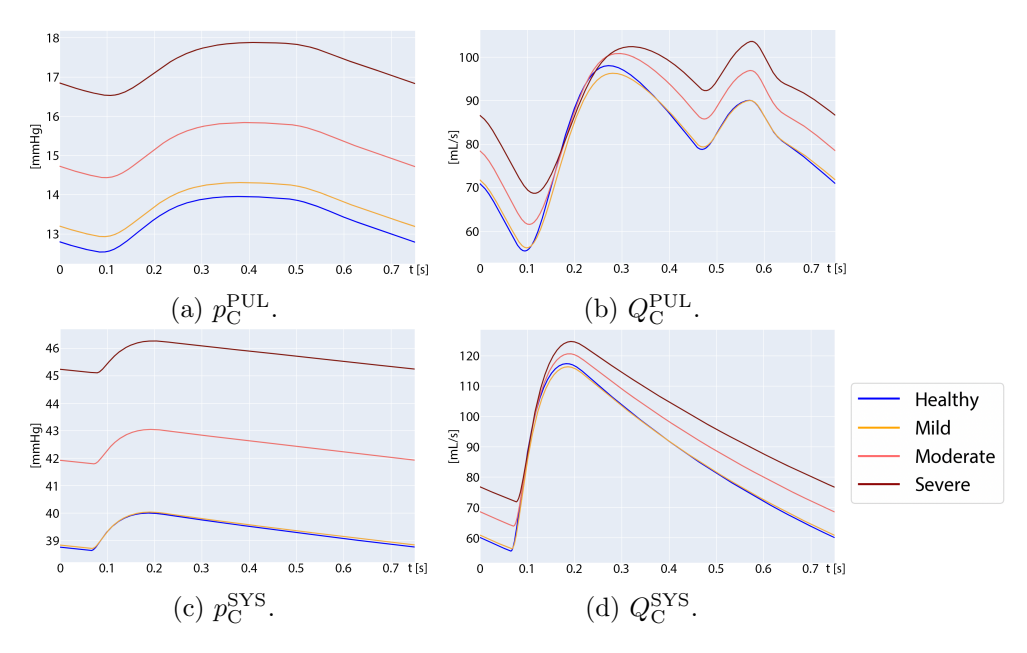


Figure 11: Time-dependent capillary variables from ( $\mathscr{C}_{\mathbb{C}}$ ). Mild, moderate and severe renovascular hypertension with secondary pulmonary hypertension (in orange, light red and dark red) is compared with a healthy individual (in blue).

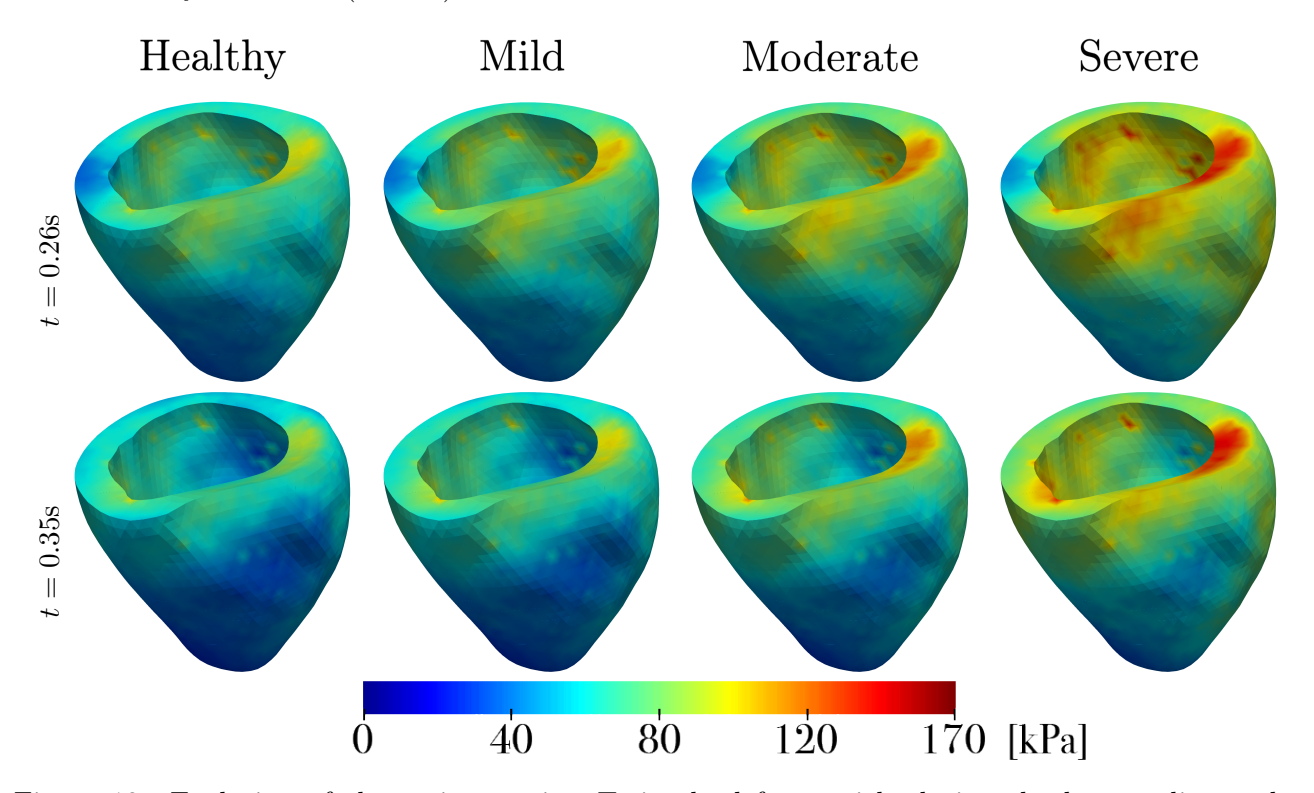


Figure 12: Evolution of the active tension  $T_a$  in the left ventricle during the last cardiac cycle. Each picture is displayed on the reference configuration  $\Omega_0$ . Mild, moderate and severe renovascular hypertension with secondary pulmonary hypertension is compared with a healthy individual.

pronounced positive and negative peaks, reflecting greater volumetric deformation of the left ventricle, with stronger dilation and more intense contraction during the cardiac cycle. These larger variations are consistent with the altered loading conditions imposed by renovascular hypertension, indicating increased mechanical stress on the ventricular myocardium.

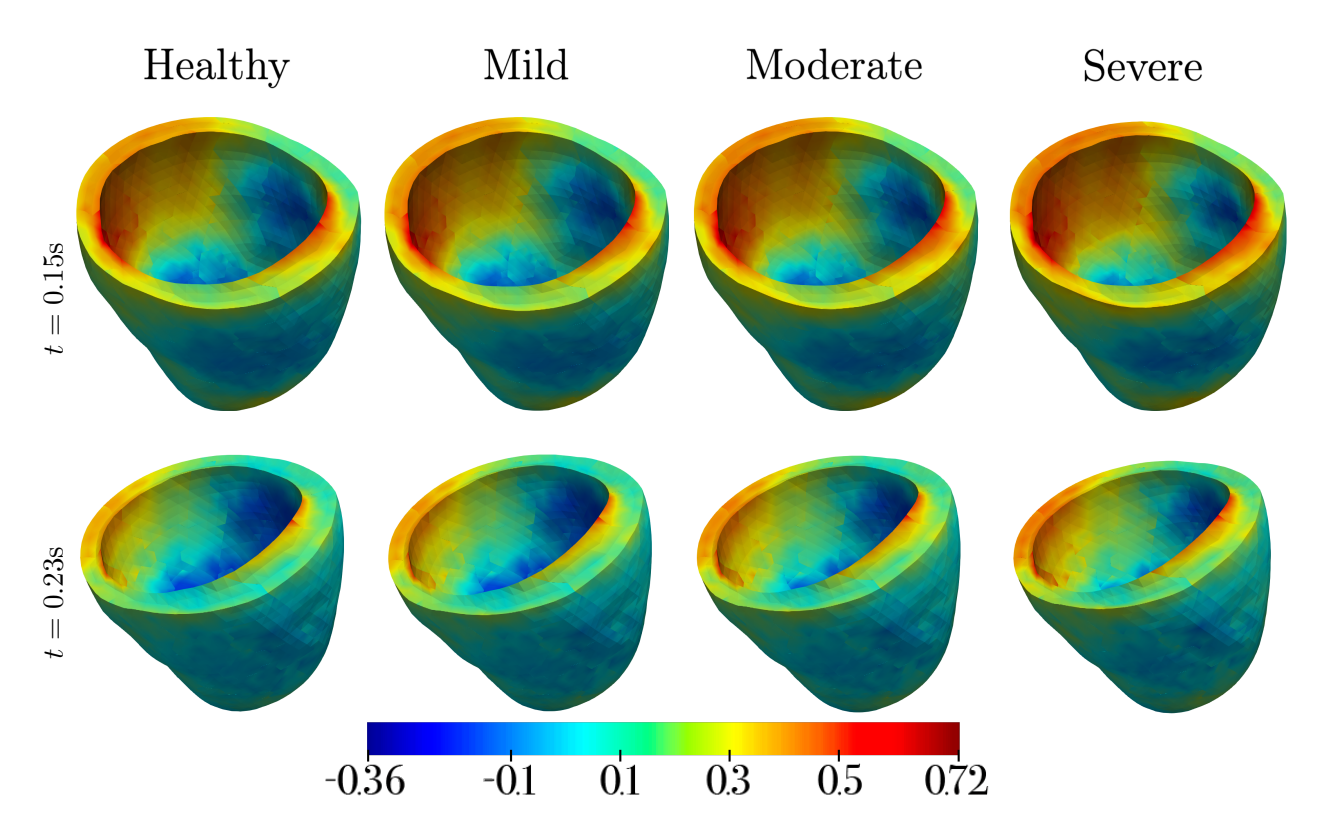


Figure 13: Evolution of the Green-Lagrange strain trace  $tr(\mathbf{E})$  in the left ventricle during the last cardiac cycle. Each picture is warped by the displacement vector  $\mathbf{d}$ . Mild, moderate and severe renovascular hypertension with secondary pulmonary hypertension is compared with a healthy individual.

#### 6 Conclusions

This work developed and applied a computational modeling framework to study hypertension in systemic, pulmonary and renovascular forms and in three nuances of severity, using both 0D models (with and without capillaries) [31] and a 3D–0D coupled model with electromechanical representation of the left ventricle [29], within a perspective that moved toward the development of cardiovascular DTs. The methodology included parameter calibration, global and multi-parametric sensitivity analysis and systematic comparison between models with and without capillaries.

The calibration approach allowed for a clear distinction between degrees of hypertension, reproducing physiological trends: increase in systolic and diastolic blood pressure, alterations in valve flows, changes in cardiac volumes and systemic venous and pulmonary pressures. The 0D model with capillaries ( $\mathscr{C}_{\mathbb{C}}$ ) demonstrated a high degree of flexibility in representing a broad spectrum of haemodynamic conditions: it was able to incorporate variations in cardiovascular parameters, consistent with the typical alterations observed in clinical cases of hypertension. The comparison with the version without capillaries ( $\mathcal{C}_{NC}$ ) showed that, by adjusting the parameters appropriately, comparable results can be obtained, confirming the robustness of the simplified model. The comparison between the 0D model and the 3D-0D model showed substantial differences in the ability to reproduce haemodynamic phenomena, especially under pathological conditions. The 3D-0D model, thanks to the three-dimensional mechanical description of the left ventricle, returned more realistic pressure-volume curves, consistent with literature clinical observations. It showed a more physiological behaviour of the cardiac index in systemic hypertension, greater sensitivity in the representation of right ventricular dysfunction in pulmonary hypertension, and better consistency of venous and arterial flows and pressures in the renovascular form. Furthermore, the spatial distribution of stresses and strains in the ventricle made it possible to pick up early signs of pathological remodeling that the more simplified 0D model tends to overlook.

Overall, the model responded positively to its objective: to represent the hypertensive condition in a realistic and robust way and to provide a foundation for patient-specific DT frameworks capable of integrating both reduced-order and high-fidelity electromechanical descriptions.

We recognize that our study has certain limitations. The calibration was conducted on synthetic data generated by ( $\mathcal{C}_{\rm C}$ ) model: it ensures a controlled comparison, but introduces the risk of not fully reflecting the individual variability of real patients. The lack of direct calibration of the 3D–0D model means that some mechanical aspects of the ventricle (particularly electrophysiological parameters and active contractility parameters) remain unoptimised and potentially less realistic, as certain physiological mechanisms regulating contraction may not be fully captured. 3D simulation requires high computational effort, limiting the number of scenarios that can be explored and its applicability in real-time clinical settings; this can be circumvented by means of reduced order models [65].

A significant extension of the work could arise from the integration of real clinical data to calibrate and validate the models. Using specific measurements, such as pressure, flow, volume, cardiac geometries, would allow the creation of true cardiovascular DTs, potentially useful for personalised diagnostics and monitoring. Such an approach requires more robust strategies to handle inter-individual variability and implement adaptive cost functions. Possible avenues of extension include 3D modeling of vascular and cardiac structures relevant in hypertension (e.g. [12, 30, 66]):

- 1. Systemic hypertension: 3D modeling of the aorta, carotids and femoral arteries to study pressure wave propagation.
- 2. Pulmonary hypertension: include right atrium, right ventricle and pulmonary vessels to better validate heart-lung interaction.
- 3. Renovascular hypertension with secondary pulmonary hypertension: add a 3D representation of the renal circulation, with dedicated arteries and veins, and the inclusion of equations describing the effect of sodium concentration on pressure control. The kidney contributes to hypertension both through diuretic and natriuretic mechanisms [67, 26] and by modulating sympathetic tone through reflexes that increase nerve activity and blood pressure [27]: these aspects are particularly important in salt-sensitive cases and in chronic conditions, particularly in renovascular hypertension.

Finally, the possibility of directly calibrating the 3D–0D model, including electromechanical parameters, shall be considered. Although computationally demanding, this extension would represent a crucial step toward DT-ready electromechanical models, bridging the gap between high-fidelity simulations and real-time personalised applications.

## Acknowledgements

AT, FR, LD and AQ are members of the INdAM group GNCS "Gruppo Nazionale per il Calcolo Scientifico" (National Group for Scientific Computing).

AT, FR and LD acknowledge the INdAM GNCS project CUP E53CE53C24001950001. FR has received support from the project FIS, MUR, Italy 2025-2028, Project code: FIS-2023-02228, CUP: D53C24005440001, "SYNERGIZE: Synergizing Numerical Methods and Machine Learning for a new generation of computational models". LD acknowledges the project PRIN2022, MUR, Italy, 2023-2025, 202232A8AN "Computational modeling of the heart: from efficient numerical solvers to cardiac digital twins".

The present research is part of the activities of "Dipartimento di Eccellenza 2023-2027", MUR, Italy, Dipartimento di Matematica, Politecnico di Milano.

#### $\mathbf{A}$ 3D-0D Model Equations

The complete 3D–0D model is defined by the set of Equations (14): Equations (14a)–(14d) are solved in the space-time domain  $\Omega_0 \times (0,T]$ , while Equation (14e) in (0,T], and Equation (14f) represents the coupling condition between 3D and 0D.

$$\begin{pmatrix}
J\chi_{\rm m} \left[ C_{\rm m} \frac{\partial u}{\partial t} + \mathcal{I}_{\rm ion}(u, \boldsymbol{w}, \boldsymbol{z}) \right] - \nabla \cdot \left( J \mathbf{F}^{-1} \mathbf{D}_{\rm M} \mathbf{F}^{-T} \nabla u \right) = J\chi_{\rm m} \mathcal{I}_{\rm app}(t), \\
\left( J \mathbf{F}^{-1} \mathbf{D}_{\rm M} \mathbf{F}^{-T} \nabla u \right) \cdot \mathbf{N} = 0 & \text{on } \partial \Omega_{0} \times (0, T], \\
u = u_{0} & \text{in } \Omega_{0} \times \{0\},
\end{pmatrix} \tag{14a}$$

$$\begin{aligned}
&\{\mathcal{E}\} \begin{cases}
J\chi_{\mathbf{m}} \left[ \mathbf{C}_{\mathbf{m}} \frac{\partial u}{\partial t} + \mathcal{I}_{\text{ion}}(u, \boldsymbol{w}, \boldsymbol{z}) \right] - \nabla \cdot \left( J \mathbf{F}^{-1} \mathbf{D}_{\mathbf{M}} \mathbf{F}^{-T} \nabla u \right) = J\chi_{\mathbf{m}} \mathcal{I}_{\text{app}}(t), \\
&\{ J \mathbf{F}^{-1} \mathbf{D}_{\mathbf{M}} \mathbf{F}^{-T} \nabla u \right) \cdot \mathbf{N} = 0 & \text{on } \partial \Omega_{0} \times (0, \mathbf{T}], \\
&u = u_{0} & \text{in } \Omega_{0} \times \{0\}, 
\end{aligned}$$

$$\begin{aligned}
&\{ \frac{\partial \boldsymbol{w}}{\partial t} - \mathbf{H}(u, \boldsymbol{w}) = \mathbf{0}, \\
&\{ \frac{\partial \boldsymbol{z}}{\partial t} - \mathbf{G}(u, \boldsymbol{w}, \boldsymbol{z}) = \mathbf{0}, \\
&\{ \boldsymbol{w} = \boldsymbol{w}_{0}, \quad \boldsymbol{z} = \boldsymbol{z}_{0} & \text{in } \Omega_{0} \times \{0\}, 
\end{aligned}$$

$$\begin{aligned}
&\{ \frac{\partial \boldsymbol{s}}{\partial t} = \mathbf{F}_{\text{act}} \left( \boldsymbol{s}, \left[ \mathbf{C} \mathbf{a}^{2+} \right]_{i}, \mathbf{SL}, \frac{\partial \mathbf{SL}}{\partial t} \right), \\
&\{ \boldsymbol{s} = \boldsymbol{s}_{0} & \text{in } \Omega_{0} \times \{0\}, 
\end{aligned}$$

$$\begin{aligned}
&\{ \rho_{s} \frac{\partial^{2} \boldsymbol{d}}{\partial t^{2}} - \nabla \cdot \mathbf{P} \left( \boldsymbol{d}, T_{a}(\boldsymbol{s}) \right) = \mathbf{0}, 
\end{aligned}$$

$$\end{aligned}$$

$$\begin{aligned}
&\{ \partial \boldsymbol{d} \\
&\{ \boldsymbol{\sigma} \mathbf{c} \\
&$$

$$(\mathscr{A}) \begin{cases} \frac{\partial \mathbf{s}}{\partial t} = \mathbf{F}_{\text{act}} \left( \mathbf{s}, \left[ \operatorname{Ca}^{2+} \right]_{i}, \operatorname{SL}, \frac{\partial \operatorname{SL}}{\partial t} \right), \\ \mathbf{s} = \mathbf{s}_{0} & \text{in } \Omega_{0} \times \{0\}, \end{cases}$$
 (14c)

$$\begin{cases}
\rho_{s} \frac{\partial^{2} \mathbf{d}}{\partial t^{2}} - \nabla \cdot \mathbf{P} \left( \mathbf{d}, T_{a}(s) \right) = \mathbf{0}, \\
\mathbf{P} \left( \mathbf{d}, T_{a}(s) \right) \mathbf{N} + \mathbf{K}^{\text{epi}} \mathbf{d} + \mathbf{C}^{\text{epi}} \frac{\partial \mathbf{d}}{\partial t} = \mathbf{0} & \text{on } \Gamma_{0}^{\text{epi}} \times (0, T], \\
\mathbf{P} \left( \mathbf{d}, T_{a}(s) \right) \mathbf{N} = p_{\text{LV}}(t) \left| J \mathbf{F}^{-T} \mathbf{N} \right| \mathbf{v}^{\text{base}} & \text{on } \Gamma_{0}^{\text{base}} \times (0, T], \\
\mathbf{P} \left( \mathbf{d}, T_{a}(s) \right) \mathbf{N} = -p_{\text{LV}}(t) J \mathbf{F}^{-T} \mathbf{N} & \text{on } \Gamma_{0}^{\text{endo}} \times (0, T], \\
\mathbf{d} = \mathbf{d}_{0}, \quad \frac{\partial \mathbf{d}}{\partial t} = \dot{\mathbf{d}}_{0} & \text{in } \Omega_{0} \times \{0\}, \\
(\mathscr{C}) \begin{cases} \frac{d\mathbf{c}_{1}(t)}{dt} = \mathbf{\widetilde{D}} \left( t, \mathbf{c}_{1}(t), p_{\text{LV}}(t) \right) & \text{in } (0, T], \\
\mathbf{c}_{1}(0) = \mathbf{c}_{1,0}, \end{cases} \\
(\mathscr{V}) V_{\text{LV}}^{\text{0D}} \left( \mathbf{c}_{1}(t) \right) = V_{\text{LV}}^{\text{3D}} \left( \mathbf{d}(t) \right) & \text{in } (0, T]. \end{cases} \tag{144}$$

$$\begin{pmatrix}
\frac{d\mathbf{c}_1(t)}{dt} = \overset{\sim}{\mathbf{D}}(t, \mathbf{c}_1(t), p_{\text{LV}}(t)) & \text{in } (0, T], \\
\mathbf{c}_1(0) = \mathbf{c}_{1,0},
\end{pmatrix} \tag{14e}$$

$$(\mathscr{V}) \quad V_{\text{LV}}^{\text{0D}}\left(\boldsymbol{c}_{1}(t)\right) = V_{\text{LV}}^{\text{3D}}\left(\boldsymbol{d}(t)\right) \qquad \text{in } (0, T]. \tag{14f}$$

#### $\mathbf{B}$ Healthy individual parameters

Parameter	i = LA	i = LV	i = RA	i = RV	Unit
$E_i^a$	0.255	8.442	$6 \cdot 10^{-2}$	0.495	m mmHg/mL
$egin{array}{c} egin{array}{c} \egin{array}{c} \egin{array}{c} \egin{array}{c} \egin{array}$	0.1512	0.126	$7 \cdot 10^{-2}$	$7\cdot 10^{-2}$	$\mathrm{mmHg/mL}$
${ m T}_{ m C}^i$	0.15	0.25	0.1	0.25	$\mathbf{s}$
$egin{array}{c} egin{array}{c} \egin{array}{c} \egin{array}{c} \egin{array}{c} \egin{array}$	0.8	0.5	0.7	0.4	$\mathbf{s}$
${ m t}_{ m C}^i$	0.75	0	0.8	0	$\mathbf{s}$
$V_{0,i}$	4	42	4	16	$\mathrm{mL}$
$R_{\min}$	$7.5\cdot 10^{-3}$	$7.5\cdot 10^{-3}$	$7.5\cdot 10^{-3}$	$7.5\cdot 10^{-3}$	$\mathrm{mmHg}\cdot\mathrm{s/mL}$
$R_{max}$	75006.2	75006.2	75006.2	75006.2	$mmHg \cdot s/mL$

Table 5: Reference parameter values for a healthy individual, used in  $(\mathscr{C}_{NC})$ , describing the heart chambers.

Parameter	i = SYS	i = PUL	$\operatorname{Unit}$
$R_{AR}^{i}$	0.42	0.104	$\mathrm{mmHg}\cdot\mathrm{s/mL}$
$\mathcal{L}_{\mathrm{AR}}^{i}$	$5 \cdot 10^{-3}$	$5\cdot 10^{-4}$	$\mathrm{mmHg}\cdot\mathrm{s}^2/\mathrm{mL}$
$\mathrm{C}_{\mathrm{AR}}^{i}$	0.96	5	$\mathrm{mL/mmHg}$
$\mathbf{R}_{\mathrm{VEN}}^{i}$	0.352	$1.05 \cdot 10^{-2}$	$\mathrm{mmHg}\cdot\mathrm{s/mL}$
$\mathcal{L}_{ ext{VEN}}^{i}$	$5 \cdot 10^{-4}$	$5 \cdot 10^{-4}$	$\mathrm{mmHg}\cdot\mathrm{s}^2/\mathrm{mL}$
$\mathrm{C}_{\mathrm{VEN}}^{i}$	60	16	$\mathrm{mL/mmHg}$

Table 6: Reference parameter values for a healthy individual, used in  $(\mathscr{C}_{NC})$ , describing the circulation.

Parameter	i = LA	i = LV	i = RA	i = RV	Unit
$E_i^a$	0.38	2.7	0.126	0.43	$\overline{\mathrm{mmHg/mL}}$
$\mathrm{E}_{i}^{p}$	0.27	$6.9 \cdot 10^{-2}$	0.195	$4.1264 \cdot 10^{-2}$	$\mathrm{mmHg/mL}$
$egin{array}{l}  ext{E}_i^p \  ext{T}_{ ext{C}}^i \  ext{T}_{ ext{R}}^i \  ext{t}_{ ext{C}}^i \end{array}$	0.1	0.265	0.1	0.3	$\mathbf{s}$
${ m T}_{ m R}^i$	0.8	0.4	0.7	0.4	$\mathbf{S}$
${ m t}_{ m C}^i$	0.75	0	0.8	0	$\mathbf{s}$
$\mathrm{V}_{0,i}$	4	3.541	3.5385	8.4067	$\mathrm{mL}$
$R_{\min}$	$6.2872 \cdot 10^{-3}$	$6.2872 \cdot 10^{-3}$	$6.2872 \cdot 10^{-3}$	$6.2872 \cdot 10^{-3}$	$\mathrm{mmHg}\cdot\mathrm{s/mL}$
$R_{max}$	94168	94168	94168	94168	$mmHg \cdot s/mL$

Table 7: Reference parameter values for a healthy individual, used in  $(\mathscr{C}_{\mathbb{C}})$ , describing the heart chambers.

Parameter	i = SYS	i = PUL	Unit
$\overline{\mathrm{R}_{\mathrm{AR}}^{i}}$	0.5911	$7.14 \cdot 10^{-2}$	$\mathrm{mmHg}\cdot\mathrm{s/mL}$
${ m L}_{ m AR}^i$	$2.0643 \cdot 10^{-4}$	$2.0643 \cdot 10^{-5}$	$\mathrm{mmHg}\cdot\mathrm{s}^2/\mathrm{mL}$
$\mathrm{C}_{\mathrm{AR}}^{i}$	1.3315	6.0043	$\mathrm{mL/mmHg}$
${ m R}_{ m VEN}^i$	0.3596	$3.75 \cdot 10^{-2}$	$\mathrm{mmHg}\cdot\mathrm{s/mL}$
$\mathcal{L}_{ ext{VEN}}^{i}$	$2.0643 \cdot 10^{-5}$	$2.0643 \cdot 10^{-5}$	$\mathrm{mmHg}\cdot\mathrm{s}^2/\mathrm{mL}$
$\mathrm{C}_{\mathrm{VEN}}^{i}$	75	13.181	$\mathrm{mL/mmHg}$

Table 8: Reference parameter values for a healthy individual, used in  $(\mathscr{C}_{\mathbb{C}})$ , describing systemic and pulmonary circulation.

Parameter		Unit
$R_{\rm C}^{\rm SYS}$	$2.17 \cdot 10^{-2}$	$mmHg \cdot s/mL$
$\mathrm{C}_{\mathrm{C}}^{\mathrm{SYS}}$	0.27981	$\mathrm{mL}/\mathrm{mmHg}$
$ m R_{C}^{ ilde{P}UL}$	$1.7538 \cdot 10^{-2}$	$\mathrm{mmHg}\cdot\mathrm{s/mL}$
$\mathrm{C}_{\mathrm{C}}^{\mathrm{PUL}}$	5.7803	$\mathrm{mL}/\mathrm{mmHg}$
$R_{SH}$	0.35174	$mmHg\cdot s/mL$
$C_{SH}$	$4.9043 \cdot 10^{-2}$	$\mathrm{mL/mmHg}$

Table 9: Reference parameter values for a healthy individual, used in  $(\mathscr{C}_{\mathbb{C}})$ , describing capillary circulation.

Note: the parameters presented in Tables 5–9 are a modification of literature values [68, 69] in such a way that the model outputs lie in the healthy individual's ranges, listed in C.

#### C Healthy individual's ranges

Output	Healthy range	Unit	Source
$LA_{IVmax}$	[24, 57]	$\mathrm{mL/m^2}$	[70]
$ m LA_{IVmin}$	[9, 28]	$\mathrm{mL/m^2}$	[70]
$LA_{IVpreAC}$	[15, 46]	$\mathrm{mL/m^2}$	[71]
$LA_{PassEF}$	[8, 44]	%	[71]
$\mathrm{LA}_{\mathrm{ActEF}}$	[17, 58]	%	[71]
$\mathrm{LA}_{\mathrm{TotEF}}$	[37, 70]	%	[70]
$LA_{Pmax}$	[6, 20]	mmHg	[72]
$\mathrm{LA}_{\mathrm{Pmin}}$	[-2, 9]	mmHg	[72]
$LA_{Pmean}$	[4, 12]	mmHg	[72]

Table 10:	Left atrium-related ranges of outputs
computed	for a healthy individual.

Output	Healthy range	$\operatorname{Unit}$	Source
RA <sub>IVmax</sub>	[28, 76]	$\mathrm{mL/m^2}$	[70]
$\mathrm{RA}_{\mathrm{IVmin}}$	[9, 45]	$\mathrm{mL/m^2}$	[70]
$RA_{IVpreAC}$	[19, 61]	$\mathrm{mL/m^2}$	[71]
$RA_{PassEF}$	[4,41]	%	[71]
$RA_{ActEF}$	[11, 55]	%	[71]
$RA_{TotEF}$	[29, 68]	%	[70]
$RA_{Pmax}$	[2, 14]	mmHg	[72]
$\mathrm{RA}_{\mathrm{Pmin}}$	[-2, 6]	mmHg	[72]
$RA_{Pmean}$	[-1, 8]	mmHg	[72]

Table 11: Right atrium-related ranges of outputs computed for a healthy individual.

Output	Healthy range	Unit	Source
$\overline{ m LV_{ISV}}$	[30, 66]	$\mathrm{mL/m^2}$	[70]
$\mathrm{LV}_{\mathrm{IEDV}}$	[47, 107]	$\mathrm{mL/m^2}$	[70]
$LV_{\rm IESV}$	[11, 47]	$\mathrm{mL/m^2}$	[70]
$\mathrm{LV}_{\mathrm{EF}}$	[51, 76]	%	[70]
$LV_{Pmax}$	[90, 140]	mmHg	[72]
$\mathrm{LV}_{\mathrm{Pmin}}$	[4, 12]	mmHg	[72]

Table 12: Left ventricle-related ranges of outputs computed for a healthy individual.

Output	Healthy range	Unit	Source
$\overline{ m RV}_{ m ISV}$	[28, 75]	$\mathrm{mL/m^2}$	[70]
$\mathrm{RV}_{\mathrm{IEDV}}$	[53, 123]	$\mathrm{mL/m^2}$	[70]
$RV_{IESV}$	[17, 59]	$\mathrm{mL/m^2}$	[70]
$\mathrm{RV}_{\mathrm{EF}}$	[42, 72]	%	[70]
$RV_{Pmax}$	[15, 28]	mmHg	[72]
$\mathrm{RV}_{\mathrm{Pmin}}$	[0, 8]	mmHg	[72]

Table 13: Right ventricle-related ranges of outputs computed for a healthy individual.

Output	Healthy range	$\operatorname{Unit}$	Source
CI	[2.8, 4.2]	$\mathrm{m}^2\cdot\mathrm{L/min}$	[72]
$SAP_{max}$	[0, 140]	$\mathrm{mmHg}$	[73]
$\mathrm{SAP}_{\mathrm{min}}$	[0, 80]	$\mathrm{mmHg}$	[73]
$PAP_{max}$	[15, 28]	$\mathrm{mmHg}$	[72]
$PAP_{\min}$	[5, 16]	$\mathrm{mmHg}$	[72]
$PAP_{mean}$	[10, 22]	$\mathrm{mmHg}$	[72]
$PWP_{max}$	[9, 23]	$\mathrm{mmHg}$	[72]
$PWP_{\min}$	[1, 12]	$\mathrm{mmHg}$	[72]
$PWP_{mean}$	[6, 15]	$\mathrm{mmHg}$	[72]
SVR	[11.3, 17.5]	$\mathrm{mmHg}\cdot\mathrm{min}/\mathrm{L}$	[72]
PVR	[1.9, 3.1]	$\mathrm{mmHg}\cdot\mathrm{min}/\mathrm{L}$	[72]
$\mathrm{S}_f$	[0, 0.05]	$1/\mathrm{m}^2$	[74]

Table 14: Further ranges of outputs computed for a healthy individual.

Note: the ranges presented in Tables 10–14 are derived from echocardiography (the ones taken from [73, 72]) and magnetic resonance imaging (MRI) (the ones taken from [70, 71]), meaning that using general healthy ranges may not always be entirely appropriate; however, this is not an issue since, despite the differences between echocardiography and MRI, the quantities computed by both ( $\mathcal{C}_{NC}$ ) and ( $\mathcal{C}_{C}$ ) for a healthy individual fall within all ranges.

#### Algorithm 1 Parameter matching algorithm for capillary and non-capillary 0D models

```
1: Input: \boldsymbol{\theta}_0^{\text{C}}, \boldsymbol{\theta}_0^{\text{NC}}, n, k
 2: Output: \boldsymbol{\theta}_0, \varepsilon
3: \boldsymbol{\theta}_0 \longleftarrow \left[\boldsymbol{\theta}_0^{\mathrm{C}}, \boldsymbol{\theta}_0^{\mathrm{NC}}\right]
  4: MNC \leftarrow 0DMODELNOCAPILLARY(\boldsymbol{\theta}_{0}^{\text{NC}})
  5: MC \leftarrow 0DMODELCAPILLARY(\boldsymbol{\theta}_0)
  6: \varepsilon \leftarrow \text{ComputeError}(\text{MNC}, \text{MC})
  7: for \theta \in \boldsymbol{\theta}_0 do
            for j = 1, \ldots, n do
                 \bar{\theta} \longleftarrow \theta \cdot k
 9:
                 MC \leftarrow 0DMODELCAPILLARY(UPDATEPARAMETER(\bar{\theta}, \theta_0))
10:
                 \delta \leftarrow \text{ComputeError}(\text{MNC}, \text{MC})
11:
                 if \delta < \varepsilon then
12:
                      \boldsymbol{\theta}_0 \longleftarrow \text{UpdateParameter}(\bar{\boldsymbol{\theta}}, \boldsymbol{\theta}_0)
13:
14:
15:
                 else
                      break
16:
                 end if
17:
            end for
19: end for
20: return \theta_0, \varepsilon
```

#### D Parameter Tuning for Cross-Model Equivalence

When comparing two sets of output coming from simulations carried on with different 0D models, it is essential to assess whether the presence of capillaries introduces significant variations that compromise the validity of the comparison. The idea is to determine the parameters of  $(\mathscr{C}_{C})$  such that its simulated outputs are as close as possible to those obtained from  $(\mathscr{C}_{NC})$ . For this purpose, Algorithm 1 has been implemented. Firstly, a set of parameters  $\boldsymbol{\theta}_{0}^{NC}$  is chosen for  $(\mathscr{C}_{NC})$ , and a simulation (MNC) is performed. Then, a simulation (MC) is executed by means of  $(\mathscr{C}_{C})$ : in this case, the same parameter set  $\boldsymbol{\theta}_{0}^{NC}$  is employed, with the addition of values corresponding to capillary circulation parameters, denoted by  $\boldsymbol{\theta}_{0}^{C}$ . The initial tolerance  $\varepsilon$  is calculated as the error between the outputs of these two simulations in the following way:

$$\varepsilon = \sum_{\alpha \in A} \frac{\delta V_{\alpha}}{\log\left(2 + \overline{V}_{\alpha}^{C}\right)},\tag{15}$$

where:

$$\delta V_{\alpha} = \int_{\mathrm{T-T_{HB}}}^{\mathrm{T}} \left| V_{\alpha}^{\mathrm{NC}}(t) - V_{\alpha}^{\mathrm{C}}(t) \right| \, dt, \qquad \qquad \overline{V}_{\alpha}^{\mathrm{C}} = \frac{1}{\mathrm{T_{HB}}} \int_{\mathrm{T-T_{HB}}}^{\mathrm{T}} \left| V_{\alpha}^{\mathrm{C}}(t) \right| \, dt,$$

with  $\{V_{\alpha}\}_{\alpha\in A}$  being the set of variable that contribute to the error computation; it comprehends a total of 20 variables: pressures and volumes of the four heart chambers, pressures and fluxes of systemic and pulmonary (arterial and venous) circulation, and fluxes through the four heart valves. Having defined the initial guess  $\boldsymbol{\theta}_0 = [\boldsymbol{\theta}_0^{\rm C}, \boldsymbol{\theta}_0^{\rm NC}]$ , the parameters of  $(\mathcal{C}_{\rm C})$  are adjusted iteratively: each parameter  $\theta$  is modified individually using a scaling coefficient k. After each modification, a new simulation of MC is performed, and the error  $\delta$  is computed as the distance between the outputs of MNC and the current MC, using Equation (15). If the new error is smaller than that of the previous step, the current parameter  $\theta$  is updated (line 13 in Algorithm 1; the function UPDATEPARAMETER( $\bar{\theta}, \boldsymbol{\theta}_0$ ) takes as input  $\bar{\theta}$  and  $\boldsymbol{\theta}_0$ , and returns as output the new set of parameters, in which  $\theta$  has been replaced with  $\bar{\theta}$ ), and the previous error  $\varepsilon$  is replaced with the new one. This procedure is repeated n times for each parameter.

In order to reduce the error between the outputs of the two simulations below a desired threshold, the whole algorithm has to be iterated several times, for different values of n and k. Specifically, k

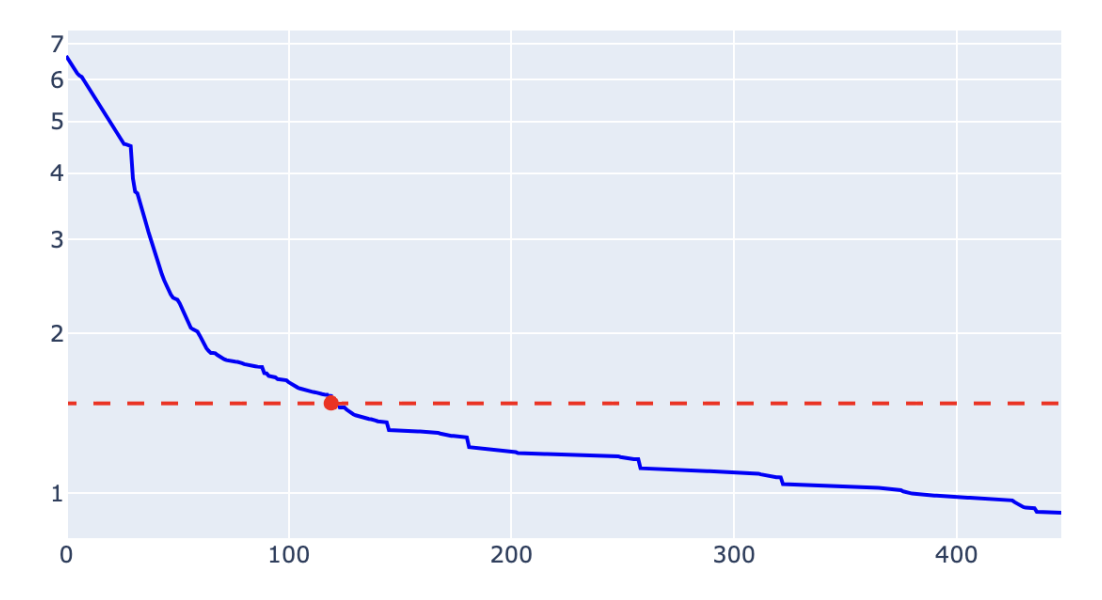


Figure 14: Evolution of the error (in blue) measuring the distance between the output variables of  $(\mathcal{C}_{NC})$  and  $(\mathcal{C}_{C})$ , as a function of the number of iterations, until it reaches 0.92. The y-axis is in logarithmic scale. The red point indicates the iteration where the error falls below the threshold of 1.5, which is considered an acceptable value.

is chosen within a neighbourhood of 1 ( $k \in U(1)$ ), alternating between values greater and less than 1: this ensures that parameters can be either increased or decreased as needed. It is also possible to apply the algorithm backwards, adapting the parameters of the ( $\mathcal{C}_{NC}$ ) so that its output variables are as close as possible to those of the ( $\mathcal{C}_{C}$ ). In this way, depending on the application to be made or the model that is used as reference, the procedure can be flexibly applied in either direction. A strict threshold of 0.92 is chosen, since reaching a lower threshold becomes computationally expensive without significantly reducing the error; furthermore, a second threshold of 1.5 is adopted, representing a good balance between computational cost and quality of the parameters. The whole analysis has been performed on a MacBook Pro (Apple M1 Pro, 10 cores, 3.2 GHz, 16 GB RAM); typically, the entire process takes only a few hundreds of iterations, in which the parameter set  $\theta_0$  is effectively updated (lines 12–14 in Algorithm 1): the reason is partly because the same starting parameter set,  $\theta_0^{NC}$ , is employed for both models ( $\mathcal{C}_{NC}$ ) and ( $\mathcal{C}_{C}$ ), hence the variables are already sufficiently close at the first step.

In order to highlight the versatility of Algorithm 1, an example is provided in which the goal is optimizing parameters of ( $\mathcal{C}_{C}$ ) in such a way that it minimizes deviations of its output variables from the reference model ( $\mathcal{C}_{NC}$ ). As shown in Figure 14, to achieve an error below the specified threshold of 0.92, approximately 76 minutes are required; nevertheless, an acceptable solution, defined as one having an error less than 1.5, is already obtained in 16 minutes. Importantly, all time-independent outputs stay within healthy ranges (C for more information about the healthy ranges), validating the adjusted parameters. To reduce the computation time even further, it is possible to remove some variables from the matching process, or the tolerance may be increased, depending on the desired accuracy. The values of the parameters used in this example as initial guess are provided in B, while the changes applied to the parameters of ( $\mathcal{C}_{C}$ ) are shown in Table 1.

In conclusion, the outputs from  $(\mathscr{C}_{C})$  and  $(\mathscr{C}_{NC})$  can be compared reliably since, by adjusting the parameters of one model to the other, very similar results can be achieved.

#### References

- [1] World Health Organization. Global report on hypertension: the race against a silent killer. Technical report, 2023. Accessed: 8 Dec. 2024.
- [2] World Health Organization. Global report on hypertension 2025: high stakes: turning evidence into action. Technical report, 2025. Accessed: 13 Oct. 2025.
- [3] M.H. Olsen, S.Y. Angell, S. Asma, P. Boutouyrie, D. Burger, J.A. Chirinos, et al. A call to action and a lifecourse strategy to address the global burden of raised blood pressure on current and future generations: the Lancet Commission on hypertension. *Lancet*, 388(10060):2665–2712, Nov. 2016.
- [4] B. Zhou, P. Perel, G.A. Mensah, and M. Ezzati. Global epidemiology, health burden and effective interventions for elevated blood pressure and hypertension. *Nat. Rev. Cardiol.*, 18(11):785–802, Nov. 2021.
- [5] Global Burden of Disease Collaborative Network. 2019 Global Burden of Disease study results, 2020. Accessed: 10 Dec. 2024.
- [6] NCD Risk Factor Collaboration (NCD-RisC). Worldwide trends in hypertension prevalence and progress in treatment and control from 1990 to 2019: a pooled analysis of 1201 populationrepresentative studies with 104 million participants. *Lancet*, 398(10304):957–980, Sep. 2021.
- [7] G. Coorey, G.A. Figtree, D.F. Fletcher, and J. Redfern. The health digital twin: advancing precision cardiovascular medicine. *Nat. Rev. Cardiol.*, 18(12):803–804, Dec. 2021.
- [8] P.M. Thangaraj, S.H. Benson, E.K. Oikonomou, F.W. Asselbergs, and R. Khera. Cardiovascular care with digital twin technology in the era of generative artificial intelligence. *Eur. Heart J.*, 45(45):4808–4821, Sep.t 2024.
- [9] G. Coorey, G.A. Figtree, D.F. Fletcher, J. Redfern, V.J. Snelson, S.T. Vernon, et al. The health digital twin to tackle cardiovascular disease-a review of an emerging interdisciplinary field. *NPJ Digit. Med.*, 5(1):126, Aug. 2022.
- [10] W. Ji, Y. Zhang, Y. Cheng, Y. Wang, and Y. Zhou. Development and validation of prediction models for hypertension risks: A cross-sectional study based on 4,287,407 participants. Front. Cardiovasc. Med., 9:928948, Sep. 2022.
- [11] W. Chang, Y. Liu, Y. Xiao, X. Yuan, X. Xu, S. Zhang, et al. A Machine-Learning-Based Prediction Method for Hypertension Outcomes Based on Medical Data. *Diagnostics*, 9(4):178, Nov. 2019.
- [12] M. Celant, E.F. Toro, G. Bertaglia, S. Cozzio, V. Caleffi, A. Valiani, et al. Modeling essential hypertension with a closed-loop mathematical model for the entire human circulation. *Int. J. Numer. Methods Biomed. Eng.*, 39(11):e3748, Nov. 2023.
- [13] B.A. Zambrano, N. McLean, X. Zhao, J.L. Tan, L. Zhong, C.A. Figueroa, et al. Patient-specific computational analysis of hemodynamics and wall mechanics and their interactions in pulmonary arterial hypertension. *Front. Bioeng. Biotechnol.*, 8:611149, Jan. 2021.
- [14] Marco Fedele, Roberto Piersanti, Francesco Regazzoni, Matteo Salvador, Pasquale Claudio Africa, Michele Bucelli, Alberto Zingaro, Luca Dede', and Alfio Quarteroni. A comprehensive and biophysically detailed computational model of the whole human heart electromechanics. Computer Methods in Applied Mechanics and Engineering, 410:115983, 2023.
- [15] G. Mancia, R. Kreutz, M. Brunström, M. Burnier, G. Grassi, A. Januszewicz, et al. 2023 ESH Guidelines for the management of arterial hypertension The Task Force for the management

- of arterial hypertension of the European Society of Hypertension: Endorsed by the International Society of Hypertension (ISH) and the European Renal Association (ERA). *J. Hypertens.*, 41(12):1874–2071, Sep. 2023. Erratum in: *Journal of Hypertension*, 42(1):194, Jan. 2024.
- [16] I. Hajjar and T.A. Kotchen. Trends in prevalence, awareness, treatment, and control of hypertension in the United States, 1988-2000. J. Am. Med. Assoc., 290(2):199–206, Jul. 2003.
- [17] M. Humbert, G. Kovacs, M.M. Hoeper, R. Badagliacca, R.M.F. Berger, M. Brida, et al. 2022 ESC/ERS Guidelines for the diagnosis and treatment of pulmonary hypertension. *Eur. Heart J.*, 43(38):3618–3731, Oct. 2022. Erratum in: *Eur. Heart J.*, 44(15):1312, Apr. 2023.
- [18] S.C. Textor. Renal arterial disease and hypertension. *Med. Clin. North Am.*, 101(1):65–79, Jan. 2017.
- [19] J.W. McEvoy, C.P. McCarthy, R.M. Bruno, S. Brouwers, M.D. Canavan, C. Ceconi, et al. 2024 ESC Guidelines for the management of elevated blood pressure and hypertension: Developed by the task force on the management of elevated blood pressure and hypertension of the European Society of Cardiology (ESC) and endorsed by the European Society of Endocrinology (ESE) and the European Stroke Organisation (ESO). *Eur. Heart J.*, 45(38):3912–4018, Oct. 2024. Supplementary data are available.
- [20] Merriam-Webster. Autoregulation. Accessed: 18 Dec. 2024.
- [21] Q. Li, J.-Y. Youn, and H. Cai. Mechanisms and consequences of endothelial nitric oxide synthase dysfunction in hypertension. *J. Hypertens.*, 33(6):1128–1136, Jun. 2015.
- [22] B. Folkow, G. Griyby, and O. Thulesius. Adaptive Structural Changes of the Vascular Walls in Hypertension and their Relation to the Control of the Peripheral Resistance. *Acta Physiol. Scand.*, 44(3-4):255–272, Dec. 1958.
- [23] L.L. Cooper, J. Rong, E.J. Benjamin, M.G. Larson, D. Levy, J.A. Vita, et al. Components of Hemodynamic Load and Cardiovascular Events: the Framingham Heart Study. *Circulation*, 131(4):354–361, Jan. 2015.
- [24] M. Nazarzadeh, A.C. Pinho-Gomes, K. Smith Byrne, D. Canoy, F. Raimondi, J.R. Ayala Solares, et al. Systolic blood pressure and risk of valvular heart disease: a Mendelian randomization study. *J. Am. Med. Assoc.*, 4(8):788–795, Aug. 2019.
- [25] R.S. Vasan, S. Pan, V. Xanthakis, A. Beiser, M.G. Larson, S. Seshadri, et al. Arterial stiffness and long-term risk of health outcomes: the Framingham Heart Study. *Hypertension*, 79(5):1045–1056, May 2022.
- [26] A.A. McDonough and M.T.X. Nguyen. Maintaining Balance Under Pressure: Integrated Regulation of Renal Transporters During Hypertension. *Hypertension*, 66(3):450–455, Jun. 2015.
- [27] G.F. DiBona. Neural control of the kidney: functionally specific renal sympathetic nerve fibers. Am. J. Physiol. Regul. Integr. Comp. Physiol., 279(5):R1517–R1524, Nov. 2000.
- [28] A.K. Bidani and K.A. Griffin. Pathophysiology of hypertensive renal damage: implications for therapy. *Hypertension*, 44(5):595–601, Nov. 2004.
- [29] F. Regazzoni, M. Salvador, P.C. Africa, M. Fedele, L. Dede', and A.M. Quarteroni. A cardiac electromechanical model coupled with a lumped-parameter model for closed-loop blood circulation. J. Comput. Phys., 457:111083, May 2022.
- [30] A.M. Quarteroni, L. Dede', F. Regazzoni, and C. Vergara. A mathematical model of the human heart suitable to address clinical problems. *Jpn. J. Ind. Appl. Math.*, 40(3):1547–1567, Sep. 2023.

- [31] A. Tonini, C. Vergara, F. Regazzoni, L. Dede', R. Scrofani, C. Cogliati, et al. A mathematical model to assess the effects of COVID-19 on the cardiocirculatory system. *Sci. Rep.*, 14(1):8304, Apr. 2024.
- [32] P. Colli Franzone, L.F. Pavarino, and G. Savaré. Computational electrocardiology: mathematical and numerical modeling. In *Complex Systems in Biomedicine*, pages 187–241. Springer, Milano, 1<sup>st</sup> edition, Dec. 2006.
- [33] P. Colli Franzone, L.F. Pavarino, and S. Scacchi. A Numerical Study of Scalable Cardiac Electro-Mechanical Solvers on HPC Architectures. *Front. Physiol.*, 9:268, Apr. 2018.
- [34] M. Potse, B. Dubé, J. Richer, A. Vinet, and R.M. Gulrajani. A comparison of monodomain and bidomain reaction-diffusion models for action potential propagation in the human heart. *IEEE Trans. Biomed. Eng.*, 53(12 Pt 1):2425–2435, Dec. 2006.
- [35] P. Colli Franzone, L.F. Pavarino, and S. Sacchi. Mathematical Cardiac Electrophysiology. Springer, Milano, 1<sup>st</sup> edition, Oct. 2014.
- [36] D. Durrer, R.T. van Dam, G.E. Freud, M.J. Janse, F.L. Meijler, and R.C. Arzbaecher. Total excitation of the isolated human heart. *Circulation*, 41(6):899–912, Jun. 1970.
- [37] M. Carue and T. Truskinovsky. Physics of muscle contraction. Rep. Prog. Phys., 81(3):036602, Mar. 2018.
- [38] F. Regazzoni, L. Dede', and A.M. Quarteroni. Biophysically detailed mathematical models of multiscale cardiac active mechanics. *PLoS Comput. Biol.*, 16(10):1–42, Oct. 2020.
- [39] J.M. Guccione, A.D. McCulloch, and L.K. Waldman. Passive material properties of intact ventricular myocardium determined from a cylindrical model. *J. Biomech. Eng.*, 113(1):42–55, Feb. 1991.
- [40] J.M. Guccione and A.D. McCulloch. Finite Element Modeling of Ventricular Mechanics. In Theory of Heart: Biomechanics, Biophysics, and Nonlinear Dynamics of Cardiac Function, pages 121–144. Springer, New York, 1<sup>st</sup> edition, Jun. 1991.
- [41] S. Doll and K. Schweizerhof. On the Development of Volumetric Strain Energy Functions. *J. Appl. Mech.*, 67(1):17–21, Oct. 1999.
- [42] M. Salvador, L. Dede', and A.M. Quarteroni. An intergrid transfer operator using radial basis functions with application to cardiac electromechanics. *Comput. Mech.*, 66(2):491–511, Aug. 2020.
- [43] Zygote Media Group Inc. Zygote Solid 3D heart generation II. Accessed: 19 Jan. 2025.
- [44] P.C. Africa. life<sup>x</sup>: A flexible, high performance library for the numerical solution of complex finite element problems. *SoftwareX*, 20:101252, Dec. 2022.
- [45] life<sup>x</sup> homepage. Accessed: 26 Feb. 2025.
- [46] M. Bucelli. The lifex library version 2.0, Nov. 2024. Accessed: 19 Jan. 2025.
- [47] A. Saltelli, M. Ratto, T. Andres, F. Campolongo, J. Cariboni, D. Gatelli, et al. *Global Sensitivity Analysis*. The Primer. Wiley-Interscience, New York, 1<sup>st</sup> edition, Jan. 2008.
- [48] A. Tonini, F. Regazzoni, M. Salvador, L. Dede', R. Scrofani, L. Fusini, et al. Two new calibration techniques of lumped-parameter mathematical models for the cardiovascular system. *Int. J. Numer. Methods Eng.*, 126(1):e7648, Jan. 2025.
- [49] J. Cheng and M. J. Druzdzel. Computational investigation of low-discrepancy sequences in simulation algorithms for bayesian networks. In *Proceedings of the Sixteenth Conference on Uncertainty in Artificial Intelligence*, pages 72–81, San Francisco, 2000. Morgan Kaufmann Publ. Inc.

- [50] A. Saltelli, P. Annoni, I. Azzini, F. Campolongo, M. Ratto, and S. Tarantola. Variance based sensitivity analysis of model output. Design and estimator for the total sensitivity index. *Comput. Phys. Commun.*, 181(2):259–270, Feb. 2010.
- [51] J.W. Gerringer, J.C. Wagner, D. Vélez-Rendón, and D. Valdez-Jasso. Lumped-parameter models of the pulmonary vasculature during the progression of pulmonary arterial hypertension. *Physiol. Rep.*, 6(3):e13586, Feb. 2018.
- [52] L. Garber, S. Khodaei, and Z. Keshavarz-Motamed. The Critical Role of Lumped Parameter Models in Patient-Specific Cardiovascular Simulations. Arch. Comput. Methods Eng., 29(5):2977–3000, Aug. 2022.
- [53] N.L. Bjørdalsbakke, J. Sturdy, E.M.L. Ingeström, and L.R. Hellevik. Monitoring variability in parameter estimates for lumped parameter models of the systemic circulation using longitudinal hemodynamic measurements. *Biomed. Eng. Online*, 22(1):34, Apr. 2023.
- [54] M. Salvador, F. Regazzoni, L. Dede', and A.M. Quarteroni. Fast and robust parameter estimation with uncertainty quantification for the cardiac function. *Comput. Methods Programs Biomed.*, 231:107402, Feb. 2023.
- [55] R.H. Byrd, P. Lu, J. Nocedal, and C. Zhu. A Limited Memory Algorithm for Bound Constrained Optimization. SIAM J. Sci. Comput., 16(5):1190–1208, 1995.
- [56] P. Virtanen, R. Gommers, T.E. Oliphant, M. Haberland, T. Reddy, D. Cournapeau, et al. SciPy 1.0: Fundamental Algorithms for Scientific Computing in Python. *Nat. Methods*, 17:261–272, Mar. 2020.
- [57] B.H. Lorell and B.A. Carabello. Left ventricular hypertrophy: pathogenesis, detection, and prognosis. *Circulation*, 102(4):470–479, Jul. 2000.
- [58] A. Salahuddin, W.S. Aronow, and Spevack D.M. At what flow rate does the aortic valve gradient become severely elevated? implications for guideline recommendations on aortic valve area cutoffs. *Arch. Med. Sci.*, 20(3):713–718, Mar. 2021.
- [59] Z. Xiajuan, D. Ding, H. Yanyan, and Zhen H. Impedance cardiographic hemodynamic variables and hypertension in elderly han residents. *Ups. J. Med. Sci.*, 118(2):80–86, Jan. 2013.
- [60] J.M. Guccione, G.S. Le Prell, P.P. de Tombe, and W.C. Hunter. Measurements of active myocardial tension under a wide range of physiological loading conditions. *J. Biomech.*, 30(2):189–192, Feb. 1997.
- [61] A. Vonk-Noordegraaf and N. Westerhof. Describing right ventricular function. Eur. Respir. J., 41(6):1419–1423, Jun. 2013.
- [62] G. Csósza, L. Valkó, E. Dinya, G. Losonczy, V. Müller, Z. Lázár, et al. Right ventricular stroke work index in pulmonary arterial hypertension and chronic thromboembolic pulmonary hypertension: A retrospective observational study. *Pulm Circ.*, 14(4):e12433, Dec. 2024.
- [63] M.J. Richter, S. Hsu, A. Yogeswaran, F. Husain-Syed, I. Vadász, H.A. Ghofrani, et al. Right ventricular pressure-volume loop shape and systolic pressure change in pulmonary hypertension. Am. J. Physiol. Lung. Cell. Mol. Physiol., 320(5):L715-L725, Mar. 2021.
- [64] D. Sun, A. Eirin, B. Ebrahimi, S.C. Textor, A. Lerman, and L.O. Lerman. Early atherosclerosis aggravates renal microvascular loss and fibrosis in swine renal artery stenosis. *J. Am. Soc. Hypertens.*, 10(4):325–335, Apr. 2016.
- [65] F. Regazzoni, S Pagani, M Salvador, L Dede', and A.M. Quarteroni. Learning the intrinsic dynamics of spatio-temporal processes through latent dynamics networks. *Nat. Commun.*, 15(1):1834, Feb. 2024.

- [66] R. Piersanti, F. Regazzoni, M. Salvador, A.F. Corno, L. Dede', C. Vergara, et al. 3D–0D closed-loop model for the simulation of cardiac biventricular electromechanics. Comput. Methods Appl. Mech. Eng., 391:114607, Mar. 2022.
- [67] R. Bautista, R. Manning, F. Martinez, M. del Carmen Avila-Casado, V. Soto, A. Medina, et al. Angiotensin II-dependent increased expression of Na<sup>+</sup>-glucose cotransporter in hypertension. Am. J. Physiol. Renal Physiol., 286(1):F127–F133, Jan. 2004.
- [68] L. Dede', F. Regazzoni, C. Vergara, P. Zunino, M. Guglielmo, R. Scrofani, et al. Modeling the cardiac response to hemodynamic changes associated with COVID-19: a computational study. *Math. Biosci. Eng.*, 18(4):3364–3383, Apr. 2021.
- [69] A. Albanese, L. Cheng, M. Ursino, and N.W. Chbat. An integrated mathematical model of the human cardiopulmonary system: model development. Am. J. Physiol. Heart Circ. Physiol., 310(7):H899–H921, Apr. 2016.
- [70] N. Kawel-Boehm, S.J. Hetzel, B. Ambale-Venkatesh, G. Captur, C.J. Francois, M. Jerosch-Herold, et al. Reference ranges ("normal values") for cardiovascular magnetic resonance (CMR) in adults and children: 2020 update. *J. Cardiovasc. Magn. Reson.*, 22(1):87, Dec. 2020. Erratum in: *J. Hypertens.*, 23(1):114, Oct. 2021.
- [71] W. Li, K. Wan, Y. Han, H. Liu, W. Cheng, J. Sunand, et al. Reference value of left and right atrial size and phasic function by SSFP CMR at 3.0 T in healthy Chinese adults. *Sci. Rep.*, 7(1):3196, Jun. 2017.
- [72] J.W. Hurst, R.C. Schlant, C.E. Rackley, E.H. Sonnenblick, and N.K. Wenger. *The heart, arteries e veins*. McGraw-Hill, New York, 7<sup>th</sup> edition, Sep. 1990.
- [73] R.M. Lang, L.P. Badano, V. Mor-Avi, J. Afilalo, A. Armstrong, L. Ernande, et al. Recommendations for cardiac chamber quantification by echocardiography in adults: an update from the American Society of Echocardiography and the European Association of Cardiovascular Imaging. J. Am. Soc. Echocardiogr., 28(1):1–39.e14, Jan. 2015.
- [74] S. Velthuis, V.M. Vorselaars, C.J. Westermann, R.J. Snijder, J.J. Mager, and M.C. Post. Pulmonary shunt fraction measurement compared to contrast echocardiography in hereditary haemorrhagic telangiectasia patients: time to abandon the 100% oxygen method? *Respiration*, 89(2):112–118, Jan. 2015.

#### **MOX Technical Reports, last issues**

Dipartimento di Matematica Politecnico di Milano, Via Bonardi 9 - 20133 Milano (Italy)

- 63/2025 Panzeri, S.; Clemente, A.; Arnone, E.; Mateu, J.; Sangalli, L.M.

  Spatio-Temporal Intensity Estimation for Inhomogeneous Poisson Point Processes on Linear

  Networks: A Roughness Penalty Method
- 62/2025 Rigamonti, V.; Torri, V.; Morris, S. K.; Ieva, F.; Giaquinto, C.; Donà, D.; Di Chiara, C.; Cantarutti, A.; CARICE study group

  Real-World Effectiveness of Influenza Vaccination in Preventing Influenza and Influenza-Like Illness in Children
- 61/2025 Coclite, A; Montanelli Eccher, R.; Possenti, L.; Vitullo, P.; Zunino, P.

  Mathematical modeling and sensitivity analysis of hypoxia-activated drugs
- 60/2025 Antonietti, P. F.; Caldana, M.; Gentile, L.; Verani M.

  Deep Learning Accelerated Algebraic Multigrid Methods for Polytopal Discretizations of Second-Order Differential Problems
- **59/2025** Wolf, F.; Botteghi, N.; Fasel, U.; Manzoni, A. *Interpretable and efficient data-driven discovery and control of distributed systems*
- 58/2025 Pivato, C.A.; Cozzi, O.; Fontana, N.; Ieva, F., et al.

  Clinical outcomes of percutaneous coronary interventions after transcatheter aortic valve replacement
- 57/2025 Guagliardi, O.; Masci, C.; Breschi, V; Paganoni A, ; Tanelli, M.

  A Novel DNA-Inspired Framework to Study University Dropout: Insights from Politecnico di Milano
- **56/2025** Tonini, A.; Bui-Thanh, T.; Regazzoni, F.; Dede', L; Quarteroni, A. *Improvements on uncertainty quantification with variational autoencoders* 
  - Tonini, A.; Bui-Thanh, T.; Regazzoni, F.; Dede', L; Quarteroni, A. Improvements on uncertainty quantification with variational autoencoders
- 55/2025 Gimenez Zapiola, A.; Boselli, A.; Menafoglio, A.; Vantini, S.

  Hyper-spectral Unmixing algorithms for remote compositional surface mapping: a review of the state of the art